Suppression of vibration transmission in coupled systems with an inerter-based nonlinear joint

Zhuang Dong[a], Baiyang Shi[a], Jian Yang*[a], Tianyun Li[b]

[a]*Faculty of Science and Engineering, University of Nottingham Ningbo China, Ningbo 315100, PR China.*

[b]*School of Naval Architecture & Ocean Engineering, Huazhong University of Science and Technology, Wuhan 430074, PR China*

*Corresponding author: jian.yang@nottingham.edu.cn

Abstract

This study proposes an inerter-based nonlinear passive joint device and investigates its vibration suppression performance when inserted in coupled systems. The joint device comprises an axial inerter and a pair of lateral inerters creating geometric nonlinearity with the nonlinear inertance force being a function of the relative displacement, velocity, and acceleration of the two terminals. Both analytical approximations based on the harmonic balance method and numerical integrations are used to obtain the steady-state response amplitude. Force transmissibility and time-averaged energy flow variables are used as performance indices to evaluate the vibration transmission in the coupled system with subsystems representing the dominant modes of interactive engineering structures. Effects of adding the proposed joint to the force-excited subsystem or to the coupling interface of subsystems on suppression performance are examined. It is found that the insertion of the inerter-based nonlinear joint can shift and bend response peaks to lower frequencies, substantially reducing the vibration of the subsystems at prescribed frequencies. By adding the joint device, the level of vibration force and energy transmission between the subsystems can be attenuated in the interested range of excitation frequencies. It is shown that the inerter-based nonlinear joint can be used to introduce an anti-peak in the response curve and achieve substantially lower levels of the force transmission and reduced amount of energy transmission between subsystems. This work provides in-depth understanding of the effects of inerter-based nonlinear devices on vibration attenuation and benefits enhanced designs of coupled systems for better dynamic performance.

Keywords: Inerter; Vibration suppression; Geometric nonlinearity; Vibration transmission; Energy flow; Force transmissibility

1. Introduction

There has been a strong need for high-performance vibration suppression devices that can be used to reduce the vibration transmission between subsystems within dynamic systems in the forms of scientific equipment and engineering structures [1]. For instance, in built-up structures such as ships or civil engineering buildings, different parts as coupling subsystems can be connected by different types of joints. One example is that aircraft engines usually contain blade roots, under platform dampers, and flange joints [2]. Bolted joints with nonlinearity are adequately used in buildings due to slipping of contacting surfacing and opening and closure of interfacial gaps [3]. Dramatic influence over the dynamic characteristics of the integrated system might be resulted from the interfacial nonlinearities in the structure [4]. Flange joints are widely used in pipes due to ease of maintenance of connected equipment and also the flexibility of the disconnection process compared with the traditional welding [5]. It is evident that the design of the joint devices is of great importance on the vibration transmission behaviour of the integrated system. Based on whether external energy input is needed, these suppression devices are classified into active vibration control systems and passive ones [6]. The applications of the former are sometimes constrained due to the consideration of reliability issues and also control efforts required, compared to passive devices [7]. In view of this, there have been much research interest in developing and investigation new passive suppression systems so as to achieve effective attenuation of vibration transmission between subsystems of an integrated system and also the vibration level of a particular subsystem.

Many passive devices such as vibration isolators and dynamic vibration absorbers contain masses, springs and dampers and the performance associated with different design configurations has been investigated and explored. There have been much less studies on passive suppression devices with the inerter, which is a relatively recently proposed passive element. The inerter has the property that the applied force is proportional to the relative accelerations of two terminals, i.e., $F_b = b(\dot{V}_1 - \dot{V}_2)$, where F_b is the coupling inertial force, b is an intrinsic parameter of the inerter named inertance, $\dot{V}_1$ and $\dot{V}_2$ are the accelerations of two terminals [8]. The corresponding inertance effect of the rack–pinion inerter is realised according to the physical parameters of the actual design, such as the radius of gyration of the flywheel and the radii of the rack pinion, gear wheel, and flywheel pinion. Other possible inerter designs have also been proposed in the past few years. The ball–screw inerter is a modified model consisting of a screw, nut, and flywheel [9]. With the involvement of the ball screw, the linear motion of the two terminals is transformed into rotation of the flywheel, which leads to corresponding motion of the gear and flywheel. The flywheel provides a storage mechanism for kinetic energy, leading to amplification of the inertia effects. Another widely used type of design is fluid inerters, which can be readily adapted into various passive network layouts [10]. Many applications have addressed the benefits of the inerter in the realm of vibration mitigation, including automobile shock absorbers [11], landing gear systems [12], and structural vibration control [13]. There have also been many studies reported demonstrating the influence of inerters in single degree-of-freedom vibration isolators [14], dual-stage isolators [15], and laminated composite plates [16]. A recent study also shows that using inerters can lead to better damping performance of dynamic systems for a higher energy dissipation efficiency [17].

While there have been much recent attempts to investigate the dynamics of linear inerter-based passive suppression devices. There are much less studies on the use of nonlinear configurations of inerters for potential benefits in vibration suppression. It has been shown that the introduction of nonlinearity can enhance the performance of vibration isolators and dynamic vibration absorbers. For instance, conventional linear single degree-of-freedom (DOF) vibration isolators have the property that effective attenuation of force transmission is achieved only when the excitation frequency is $\sqrt{2}$ times larger than the natural frequency. This brings about a trade-off between the having a lower natural frequency to enlarge the effective isolation band and a high static supporting stiffness. Nonlinear elements can be introduced to deal with the issue, by introducing a negative stiffness mechanism to have high static stiffness and a low dynamic stiffness [1]. Nonlinear vibration absorbers can also be tailored for vibration suppression of primary systems with different types of nonlinearities [18]. However, only limited studies have exploited the potential benefits of nonlinearities arising from the use of the inerters. Experimental tests have also been performed to analyse nonlinear effects on two types of inerters including the friction [19,20,21]. Yang et al. [22] proposed an inerter-based nonlinear vibration isolator by using the geometric nonlinearity of a nonlinear inertance mechanism (NIM) created by a pair of oblique inerters. It has been shown that the NIM-based isolator provides better performance compared with conventional linear isolator.

It is noted that for performance evaluation of linear and nonlinear suppression devices, the force or displacement transmissibility has been often used as an index to describe the level of vibration transmission [23]. The time-averaged vibration energy flow variables have also been widely used for accessing the performance of linear vibration isolation systems. The vibration energy flow combines the effects of amplitudes of the velocity response and the force as well as their relative phase angle in one quantity, such that the vibration transmission within a dynamical system can be better quantified from energy viewpoint [24-26]. Various energy flow analysis approaches, such as the dynamic stiffness method [27], the receptance method [28], the mobility method [29], energy flow models based on finite element [30], a substructure method [31], a progressive approach [32], and a power flow formulation based on continuum mechanics [33] have been proposed to analyse the linear vibration control systems. Damping and mobility-based power flow mode theories have also been demonstrated to facilitate power-flow-based dynamic designs [34, 35]. In recently years, energy flow methods have also been developed to investigate the power flow behaviour of nonlinear systems, including the Duffing oscillator [36], dynamic vibration absorbers [18], and nonlinear vibration isolators [37]. Power flow characteristics and performance of single-DOF linear and nonlinear inerter-based isolators have also been investigated [14, 22].

This study proposes a nonlinear passive joint device by configuring linear inerters to achieve geometric nonlinearity. The performance of such joint in attenuations of vibrations of subsystems and also suppression of vibration transmission between subsystems when inserted in a coupled system is examined. The force transmissibility and time-averaged power flow variables are used for performance evaluation from both the viewpoint of force transmission and also vibration energy flow perspective. Both analytical approximations based on the harmonic balance methods and numerical integrations are used for the determinations of the steady-state responses and the performance indices. It will be shown that effective suppression of vibrations and vibration transmission can be achieved by inserting the proposed joint device to the coupled system. The remainder of this paper is organised as follows. In Sect. 2, the inerter-based nonlinear joint and the coupled system models will be introduced and modelled. In Sect. 3, the steady-state response is obtained by using the harmonic balance method with analytical derivation and also the alternating-frequency-time scheme (AFT) with numerical continuations. In Sect. 4, the performance indices of vibration transmission between the subsystems are defined. Both the force transmissibility as well as the time-averaged vibration energy flow variables are defined and formulated. In Sect. 5, the effects of different inerters and the positions or adding the proposed nonlinear joint on vibration transmission are examined systematically. Conclusions are provided at the end of the paper.

2. Mathematical Modelling

2.1. Inerter-based nonlinear joint

Figure 1 provides a schematic representation of the proposed inerter-based nonlinear joint created by using a pair of lateral inerters and an inerter in the axial direction [15]. The nonlinear joint has two terminals A and B. One of the ends for the two lateral inerters are hinged together at terminal A and their other ends are pinned at points C and D, which are separated horizontally by $2l_0$. The lateral inerters are with the same inertance of b_1 while the axial inerter has inertance b_0. Due to the symmetry of the nonlinear joint, its terminal B only has axial motion in the horizontal, and its displacement, velocity, and acceleration is denoted by x_b, $\dot{x}_b$ and $\ddot{x}_b$, respectively. The displacement, velocity, and acceleration of the other terminal of the nonlinear joint, terminal A is represented by x_a, $\dot{x}_a$ and $\ddot{x}_a$, respectively. The relative displacement between the two terminals A and B is defined as $\delta = x_a - x_b$. Hence, the geometric nonlinearity is introduced by the inerter-based joint, where the total force between A and B is [15]:

$$f_{\mathrm{b}}(\delta, \dot{\delta}, \ddot{\delta}\,) = b_0\ddot{\delta} + 2b_1\left(\frac{\delta^2\ddot{\delta}}{l_0^2+\delta^2} + \frac{l_0^2\delta\dot{\delta}^2}{\left(l_0^2+\delta^2\right)^2}\right) = f_{\mathrm{b1}} + f_{\mathrm{b2}}, \tag{1}$$

where

$$f_{\mathrm{b1}} = \left(b_0 + \frac{2b_1\delta^2}{l_0^2+\delta^2}\right)\ddot{\delta}\,, \quad f_{\mathrm{b2}} = 2b_1\frac{l_0^2\delta\dot{\delta}^2}{\left(l_0^2+\delta^2\right)^2}\,. \tag{2a, b}$$

Eq. (1) shows that the nonlinear inertial force by the inerter-based joint depends on the displacement, velocity, and acceleration of two moving terminals A and B.

Figure 2 shows the variations of the nonlinear inertial forces f_{b1} and f_{b2} against the relative displacement δ, velocity $\dot{\delta}$, and acceleration $\ddot{\delta}$ of the two terminals for the inerter-based nonlinear joint. The parameters are set as $b_0 = 1$ kg, $b_1 = 1$ kg and $l_0 = 1$ m. Fig. 2(a) shows that the value of f_{b1} depends on both the relative displacement δ and relative acceleration $\ddot{\delta}$ of its two terminals. It shows that the value of f_{b1} is approximately proportional to the relative acceleration $\ddot{\delta}$ of two terminals when δ/l_0 is large. This character can be demonstrated by setting δ/l_0 to infinity in Eq. (2), and the corresponding value of f_{b1} will be $(2b_1 + b_0)\ddot{\delta}$, suggesting two lateral inerters tend to orient in the horizontal direction when δ/l_0 tends to infinity. Fig. 2(b) shows the effects of relative displacement and velocity of two terminals on the nonlinear force f_{b2}. It is noted that the changes in $\dot{\delta}$ has large impact on f_{b2} when $\delta \approx 0$. However, f_{b2} tends to zero when the relative displacement of two terminals $\dot{\delta}$ becomes large.

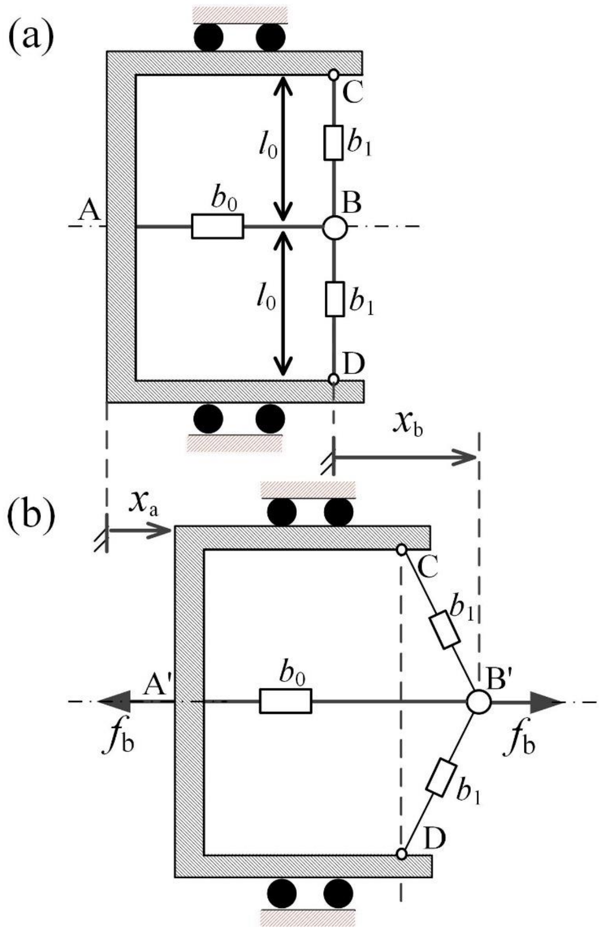

Fig. 1. Schematic representation of the inerter-based nonlinear joint.

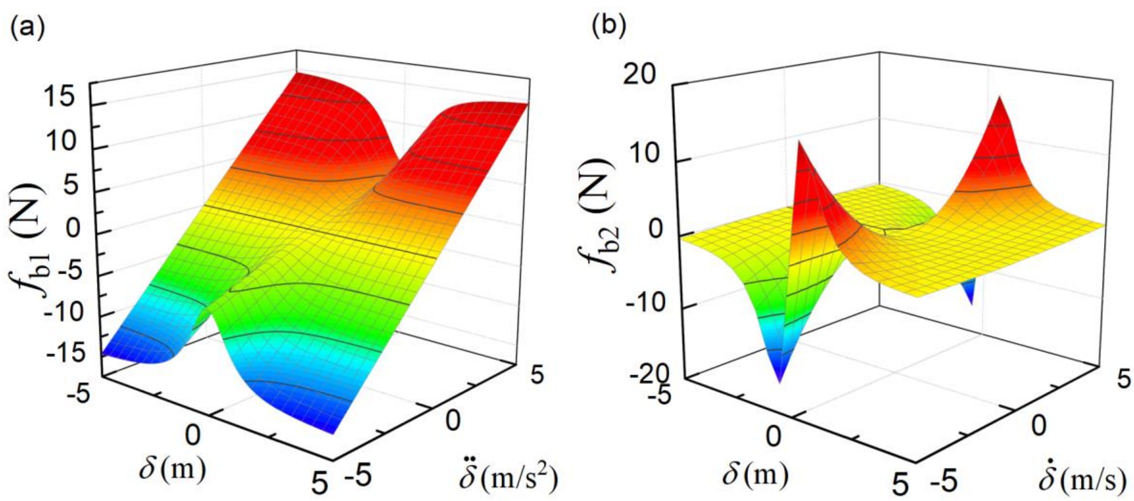

Fig. 2. Nonlinear inertial force characteristics of the inerter-based nonlinear joint ($b_0 = b_1 = 1$ kg, $l_0 = 1$ m).

2.2. Coupled system with the inerter-based joint device

Figure 3 provides a schematic representation of the model comprising two subsystems coupled with a mechanical joint characterized by a spring with stiffness coefficient k_0. Subsystem one (S1) is a single-DOF system consisting of a mass m_1 subject to an external harmonic excitation $f(t)$ of amplitude f_0 with frequency ω and phase angle ϕ, a linear spring with stiffness coefficient k_1, and a viscous damper of damping coefficient c_1. Subsystem two (S2) is another single-DOF system consisting of a mass m_2, a linear spring with stiffness coefficient k_2, and a viscous damper with damping coefficient c_2. There are also two possible positions P and Q marked in Fig. 3, for the insertion of the inerter-based nonlinear joint. It is assumed that the masses both move horizontally without frictions and their static equilibrium positions are taken as reference when $x_1 = x_2 = 0$ and the springs are upstretched.

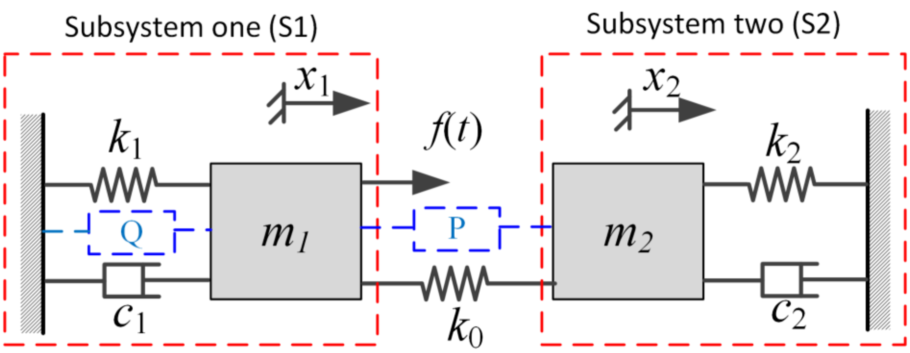

Fig. 3. A schematic representation of the coupled system with a nonlinear inerter-based joint position at positions P or Q.

When the nonlinear inerter-based joints are added at both positions P and Q, the dynamic governing equations of the system are written in a matrix form as

$$\begin{bmatrix} m_1 & 0 \\ 0 & m_2 \end{bmatrix} \begin{Bmatrix} \ddot{x}_1 \\ \ddot{x}_2 \end{Bmatrix} + \begin{bmatrix} c_1 & 0 \\ 0 & c_2 \end{bmatrix} \begin{Bmatrix} \dot{x}_1 \\ \dot{x}_2 \end{Bmatrix} + \begin{bmatrix} k_1 + k_0 & -k_0 \\ -k_0 & k_2 + k_0 \end{bmatrix} \begin{Bmatrix} x_1 \\ x_2 \end{Bmatrix} + \begin{Bmatrix} f_{\mathrm{bP}} + f_{\mathrm{bQ}} \\ -f_{\mathrm{bP}} \end{Bmatrix} = \begin{Bmatrix} f_0 \exp(\mathrm{i}(\omega t + \phi)) \\ 0 \end{Bmatrix}, \tag{3}$$

where f_{bP} and f_{bQ} represent the forces applied by the NIM-based nonlinear joint at P and Q, respectively, and are expressed by

$$f_{\mathrm{bP}} = 2b_1 \left(\frac{\delta^2 \ddot{\delta}}{{l_0}^2 + \delta^2} + \frac{l_0^2 \delta \dot{\delta}^2}{\left({l_0}^2 + \delta^2\right)^2} \right) + b_0 \ddot{\delta}, \tag{4a}$$

$$f_{\mathrm{bQ}} = 2b_1 \left(\frac{x_1^2 \ddot{x}_1}{{l_0}^2 + x_1^2} + \frac{{l_0}^2 x_1 \dot{x}_1^2}{\left({l_0}^2 + x_1^2\right)^2} \right) + b_0 \ddot{x}_1, \tag{4b}$$

where $\delta = x_1 - x_2$ is the relative displacement between the masses.

To facilitate later formulations, the following non-dimensional parameters are introduced:

$$\omega_1 = \sqrt{\frac{k_1}{m_1}},\ \omega_2 = \sqrt{\frac{k_2}{m_2}},\ \mu = \frac{m_2}{m_1},\ X_1 = \frac{x_1}{l_0},\ \ X_2 = \frac{x_2}{l_0},$$

$$\Delta = X_1 - X_2 = \frac{\delta}{l_0},\ \ \gamma = \frac{k_2}{k_1},\ \ \kappa = \frac{k_0}{k_1},\ \zeta_1 = \frac{c_1}{2m_1\omega_1},\ \ \zeta_2 = \frac{c_2}{2m_2\omega_1},$$

$$\lambda_0 = \frac{b_0}{m_1}, \quad \lambda_1 = \frac{b_1}{m_1}, \quad F_0 = \frac{f_0}{k_1 l_0}, \quad \Omega = \frac{\omega}{\omega_1}, \quad \tau = \omega_1 t, \tag{5}$$

where ω_1 and ω_2 are the undamped natural frequencies of S1 and S2, respectively, μ is the mass ratio, X_1, X_2 and Δ are the non-dimensional displacements of masses m_1, m_2, and the relative displacement between the masses, respectively, γ and κ are the stiffness ratios, ζ_1 and ζ_2 are the damping ratios, λ_0 and λ_1 are the inertance-to-mass ratios for the axial inerter and the lateral inerters in the nonlinear joint, respectively, F_0 is the non-dimensional forcing amplitude, Ω and τ are the dimensionless frequency and time, respectively.

By using these parameters and variables, the governing Eq. (1) can be written into a non-dimensional form as

$$\mathbf{M}\mathbf{X}'' + \mathbf{C}\mathbf{X}' + \mathbf{K}\mathbf{X} + \mathbf{F}_{\mathbf{nl}}(\mathbf{X}'', \mathbf{X}', \mathbf{X}) = \mathbf{F}_{\mathbf{e}}(\tau), \tag{6}$$

where $\mathbf{X} = \{X_1(\tau), X_2(\tau)\}^{\mathrm{T}}$ is the displacement response vector, $\mathbf{F}_{\mathbf{e}}(\tau) = \{F_0 \exp(\mathrm{i}\Omega\tau + \mathrm{i}\phi), 0\}^{\mathrm{T}}$ denoting the external force vector, $\mathbf{M}$, $\mathbf{C}$, and $\mathbf{K}$ represent the mass, damping and stiffness matrices of the system without adding inerter-based joints and are expressed by

$$\mathbf{M} = \begin{bmatrix} 1 & 0 \\ 0 & \mu \end{bmatrix}, \qquad \mathbf{C} = \begin{bmatrix} 2\zeta_1 & 0 \\ 0 & 2\zeta_2\mu \end{bmatrix}, \qquad \mathbf{K} = \begin{bmatrix} 1+\kappa & -\kappa \\ -\kappa & \gamma+\kappa \end{bmatrix}, \tag{7a, b, c}$$

$\mathbf{F}_{\mathbf{nl}}(\mathbf{X}'', \mathbf{X}', \mathbf{X}) = \{F_{\mathrm{bP}} + F_{\mathrm{bQ}}, \ -F_{\mathrm{bP}}\}^{\mathrm{T}}$ representing the force vector generated by the addition of the inerter-based nonlinear joint, where

$$F_{\mathrm{bP}} = 2\lambda_1 \left(\frac{\Delta^2 \Delta''}{1+\Delta^2} + \frac{\Delta {\Delta'}^2}{(1+\Delta^2)^2} \right) + \lambda_0 \Delta'', \tag{8a}$$

$$F_{\mathrm{bQ}} = 2\lambda_1 \left(\frac{X_1^2 X_1''}{1+X_1^2} + \frac{X_1 X_1'^2}{\left(1+X_1^2\right)^2} \right) + \lambda_0 X_1'', \tag{8b}$$

are the non-dimensional forces of the nonlinear joint placed at point P and point Q, respectively.

To obtain the steady-state response and vibration energy flow behaviour, it is necessary to solve the governing equations. Two methods are used in the current study. The first one is the numerical integration based on the Runge-Kutta method. The use of this method can yield accurate results with relatively high computational cost. The other method is based on analytical approximations such as the harmonic balance method (HB). The use of HB can yield the determination of stable and unstable solution branches at relatively low computation cost. The combined use of both can also facilitate validation and comparison of the results from different approaches.

3. Dynamic analysis by harmonic balance method

3.1. Analytical approximations

Here analytical approximations based on the harmonic balance method are used to obtain the steady-state frequency-response relationship the system. It is noted that for the forces created by the inerter-based nonlinear joint shown by Eq. (8) can be Taylor expanded at the equilibrium position of $\Delta = 0$ and $X_1 = 0$, respectively, to have [22]

$$F_{\mathrm{bP}} \approx \lambda_0 \Delta'' + 2\lambda_1 \Delta^2 \Delta'' + 2\lambda_1 (1 - 2\Delta^2) \Delta \Delta'^2, \tag{9a}$$

$$F_{\mathrm{bQ}} \approx \lambda_0 X_1'' + 2\lambda_1 X_1^2 X_1'' + 2\lambda_1 (1 - 2X_1^2) X_1 X_1'^2. \tag{9b}$$

Using a first order approximation, the dimensionless steady-state displacement X_1 of the mass m_1 and the relative displacement U between the two masses of the subsystems are assumed to be

$$X_1 = R_1 \exp(\mathrm{i}\Omega\tau), \qquad \Delta = U \exp(\mathrm{i}\Omega\tau + \mathrm{i}\theta), \tag{10a, b}$$

where R_1 and U represent the real amplitude of the dimensionless displacement response of mass m_1 and that of the relative displacement, respectively, θ represents difference in the phase angles of X_1 and Δ. Note that in the steady state, the phase difference between X_1 and the excitation force is denoted by ϕ. From Eq. (10a) and (b), we have the following expressions

$$X_2 = R_1 \exp(\mathrm{i}\Omega\tau) - U \exp(\mathrm{i}\Omega\tau + \mathrm{i}\theta), \quad R_2 = |X_2| = \sqrt{R_1^2 + U^2 - 2R_1 U \cos\theta}, \tag{11a, b}$$

$$X_1' = \mathrm{i}\Omega R_1 \exp(\mathrm{i}\Omega\tau), \qquad X_1'' = -\Omega^2 R_1 \exp(\mathrm{i}\Omega\tau), \tag{11c, d}$$

$$\Delta' = \mathrm{i}\Omega U \exp(\mathrm{i}\Omega\tau + \mathrm{i}\theta), \qquad \Delta'' = -\Omega^2 U \exp(\mathrm{i}\Omega\tau + \mathrm{i}\theta). \tag{11e, f}$$

where R_2 represents the dimensionless response amplitude of mass m_2. By inserting Eqs. (10) and (11) into Eq. (9) and retaining only the component at the fundamental frequency, the nonlinear forces by the inerter-based nonlinear joint are expressed by

$$F_{\mathrm{bP}} = -\left(\lambda_0 + \left(1 + \frac{U^2}{2}\right) \lambda_1 U^2\right) \Omega^2 U \exp(\mathrm{i}\Omega\tau + \mathrm{i}\theta), \tag{12a}$$

$$F_{\mathrm{bQ}} = -\left(\lambda_0 + \left(1 + \frac{R_1^2}{2}\right) \lambda_1 R_1^2\right) \Omega^2 R_1 \exp(\mathrm{i}\Omega\tau). \tag{12b}$$

Note that by using $\Delta = X_1 - X_2$ to replace X_2 in Eq. (6), it follows that

$$X_1'' + 2\zeta_1 X_1' + X_1 + \kappa\Delta + F_{\mathrm{bP}} + F_{\mathrm{bQ}} = F_0 \exp(\mathrm{i}\Omega\tau + \mathrm{i}\phi), \tag{13a}$$

$$\mu(X_1'' - \Delta'') + 2\zeta_2 \mu (X_1' - \Delta') - \kappa\Delta + \gamma(X_1 - \Delta) - F_{\mathrm{bP}} = 0. \tag{13b}$$

By using Eqs. (10), (11) and (12) to substitute the response and nonlinear force terms into Eq. (13) and balancing of the coefficients of corresponding harmonic terms, it follows that

$$\left(1 - (1 + \lambda_0)\Omega^2 + 2\zeta_1 \mathrm{i}\Omega - \left(1 + \frac{R_1^2}{2}\right) \lambda_1 R_1^2 \Omega^2\right) R_1 + \left(\kappa - \lambda_0 \Omega^2 - \left(1 + \frac{U^2}{2}\right) \lambda_1 U^2 \Omega^2\right) U \exp(\mathrm{i}\theta) = F_0 \exp(\mathrm{i}\phi), \tag{14a}$$

$$(\gamma - \mu\Omega^2 + 2\zeta_2 \mu \mathrm{i}\Omega) R_1 - \left(\gamma + \kappa - (\mu + \lambda_0)\Omega^2 + 2\zeta_2 \mu \mathrm{i}\Omega - \left(1 + \frac{U^2}{2}\right) \lambda_1 U^2 \Omega^2\right) U \exp(\mathrm{i}\theta) = 0. \tag{14b}$$

Eq. (14) is a nonlinear complex equation, and it can be further transformed into nonlinear algebraic equations by balancing the real part and imaginary part. It becomes

$$\left(1 - (1 + \lambda_0)\Omega^2 - \left(1 + \frac{R_1^2}{2}\right) \lambda_1 R_1^2 \Omega^2\right) R_1 + \left(\kappa - \lambda_0 \Omega^2 - \left(1 + \frac{U^2}{2}\right) \lambda_1 U^2 \Omega^2\right) U \cos\theta = F_0 \cos\phi, \tag{15a}$$

$$2\zeta_1 \Omega R_1 + \left(\kappa - \lambda_0 \Omega^2 - \left(1 + \frac{U^2}{2}\right) \lambda_1 U^2 \Omega^2\right) U \sin\theta = F_0 \sin\phi, \tag{15b}$$

$$(\gamma - \mu\Omega^2) R_1 - \left(\gamma + \kappa - (\mu + \lambda_0)\Omega^2 - \left(1 + \frac{U^2}{2}\right) \lambda_1 U^2 \Omega^2\right) U \cos\theta + 2\zeta_2 \mu \Omega U \sin\theta = 0, \tag{15c}$$

$$2\zeta_2\mu\Omega R_1 - \left(\gamma + \kappa - (\mu + \lambda_0)\Omega^2 - \left(1 + \frac{U^2}{2}\right)\lambda_1 U^2 \Omega^2\right) U \sin\theta - 2\zeta_2\mu\Omega U \cos\theta = 0. \quad (15d)$$

By using Eqs. (15c) and (15d) to cancel out the trigonometric terms, we have

$$(\gamma - \mu\Omega^2)^2 R_1^2 + (2\zeta_2\mu\Omega R_1)^2 = \left(\gamma + \kappa - (\mu + \lambda_0)\Omega^2 - \left(1 + \frac{U^2}{2}\right)\lambda_1 U^2 \Omega^2\right)^2 U^2 + (2\zeta_2\mu\Omega U)^2. \quad (16)$$

By treating Eqs. (15c) and (15d) as linear algebraic equations of $U \sin\theta$ and $U \cos\theta$, using the Cramer's rule, we have

$$U * R_1 \sin\theta = \frac{2\zeta_2\mu\Omega R_1^2\left(\kappa - \lambda_0\Omega^2 - \left(1 + \frac{U^2}{2}\right)\lambda_1 U^2\Omega^2\right)}{(2\zeta_2\mu\Omega)^2 + \left(\gamma + \kappa - (\mu + \lambda_0)\Omega^2 - \left(1 + \frac{U^2}{2}\right)\lambda_1 U^2\Omega^2\right)^2} \equiv A_1, \quad (17a)$$

$$U * R_1 \cos\theta = \frac{\left(\gamma + \kappa - (\mu + \lambda_0)\Omega^2 - \left(1 + \frac{U^2}{2}\right)\lambda_1 U^2\Omega^2\right)(\gamma - \mu\Omega^2) + (2\zeta_2\mu\Omega)^2}{(2\zeta_2\mu\Omega)^2 + \left(\gamma + \kappa - (\mu + \lambda_0)\Omega^2 - \left(1 + \frac{U^2}{2}\right)\lambda_1 U^2\Omega^2\right)^2} R_1^2 \equiv A_2, \quad (17b)$$

where A_1 and A_2 are introduced to enhance clarity of later formulations. A mathematical treatment of Eq. (15a) and (15b) leads to

$$\left(1 - (1 + \lambda_0)\Omega^2 - \left(1 + \frac{R_1^2}{2}\right)\lambda_1 R_1^2 \Omega^2\right)^2 R_1^2 + (2\zeta_1\Omega R_1)^2 + \left(\kappa - \lambda_0\Omega^2 - \left(1 + \frac{U^2}{2}\right)\lambda_1 U^2\Omega^2\right)^2 U^2 +$$

$$2\left(1 - (1 + \lambda_0)\Omega^2 - \left(1 + \frac{R_1^2}{2}\right)\lambda_1 R_1^2 \Omega^2\right)\left(\kappa - \lambda_0\Omega^2 - \left(1 + \frac{U^2}{2}\right)\lambda_1 U^2\Omega^2\right) A_2 + 4\zeta_1\Omega\left(\kappa - \lambda_0\Omega^2 -\right.$$

$$\left.\left(1 + \frac{U^2}{2}\right)\lambda_1 U^2\Omega^2\right) A_1 = F_0^2. \quad (18)$$

Note that Eqs. (16) and (18) are two nonlinear real algebraic equations with two unknowns R_1^2 and U^2 for the displacement amplitudes. Many methods, such as the Newton-Raphson method, are available for solving nonlinear algebraic equations. Here, a standard bisection method can be used the following procedure. Using Eqs. (16), R_1^2 can be represented by an expression of U^2:

$$R_1^2 = \frac{\left(\gamma + \kappa - (\mu + \lambda_0)\Omega^2 - \left(1 + \frac{U^2}{2}\right)\lambda_1 U^2\Omega^2\right)^2 + (2\zeta_2\mu\Omega)^2}{(\gamma - \mu\Omega^2)^2 + (2\zeta_2\mu\Omega)^2} U^2. \quad (19)$$

By inserting Eq. (19) into Eq. (18) to replace R_1^2, we have a single nonlinear algebraic equation with one known U^2. It can be solved by a standard bisection method. Subsequently, the displacement amplitude R_1 and the phase angle differences θ and ϕ can be obtained, yielding the steady-state response information. Compared with the Newton-Raphson method, the main benefit of using the bisection method is that it can conveniently determine all the possible solutions with using numerical continuation for path following.

Note that for the original coupled system without adding inerter-based joint, Eqs. (16) and (18) becomes

$$(\gamma - \mu\Omega^2)^2 R_1^2 + (2\zeta_2\mu\Omega R_1)^2 = (\gamma + \kappa - \mu\Omega^2)^2 U^2 + (2\zeta_2\mu\Omega U)^2, \quad (20a)$$

$$(1 - \Omega^2)^2 R_1^2 + (2\zeta_1\Omega R_1)^2 + \kappa^2 U^2 + 2\kappa(1 - \Omega^2) A_2 + 4\zeta_1\Omega\kappa A_1 = F_0^2, \quad (20b)$$

where

$$A_1 = \frac{2\zeta_2\mu\Omega\kappa R_1^2}{(2\zeta_2\mu\Omega)^2 + (\gamma + \kappa - \mu\Omega^2)^2}, \qquad A_2 = \frac{(\gamma + \kappa - \mu\Omega^2)(\gamma - \mu\Omega^2) + (2\zeta_2\mu\Omega)^2}{(2\zeta_2\mu\Omega)^2 + (\gamma + \kappa - \mu\Omega^2)^2} R_1^2. \quad (21a, b)$$

When the nonlinear joint is placed at point Q, we have

$$(\gamma-\mu\Omega^2)^2R_1^2+(2\zeta_2\mu\Omega R_1)^2=(\gamma+\kappa-\mu\Omega^2)^2U^2+(2\zeta_2\mu\Omega U)^2, \tag{22a}$$

$$\left(1-(1+\lambda_0)\Omega^2-\left(1+\frac{R_1^2}{2}\right)\lambda_1R_1^2\Omega^2\right)^2R_1^2+(2\zeta_1\Omega R_1)^2+\kappa^2U^2+2\left(1-(1+\lambda_0)\Omega^2-\left(1+\frac{R_1^2}{2}\right)\lambda_1R_1^2\Omega^2\right)\kappa A_2+4\zeta_1\kappa\Omega A_1=F_0^2, \tag{22b}$$

where

$$A_1=\frac{2\zeta_2\mu\Omega\kappa R_1^2}{(2\zeta_2\mu\Omega)^2+(\gamma+\kappa-\mu\Omega^2)^2},\quad A_2=\frac{(\gamma+\kappa-\mu\Omega^2)(\gamma-\mu\Omega^2)+(2\zeta_2\mu\Omega)^2}{(2\zeta_2\mu\Omega)^2+(\gamma+\kappa-\mu\Omega^2)^2}R_1^2. \tag{23a, b}$$

When the nonlinear joint is placed at point P, Eq. (14) is simplified into

$$(\gamma-\mu\Omega^2)^2R_1^2+(2\zeta_2\mu\Omega R_1)^2=\left(\gamma+\kappa-(\mu+\lambda_0)\Omega^2-\left(1+\frac{U^2}{2}\right)\lambda_1U^2\Omega^2\right)^2U^2+(2\zeta_2\mu\Omega U)^2, \tag{24a}$$

$$(1-\Omega^2)^2R_1^2+(2\zeta_1\Omega R_1)^2+\left(\kappa-\lambda_0\Omega^2-\left(1+\frac{U^2}{2}\right)\lambda_1U^2\Omega^2\right)^2U^2+2(1-\Omega^2)\left(\kappa-\lambda_0\Omega^2-\left(1+\frac{U^2}{2}\right)\lambda_1U^2\Omega^2\right)A_2+4\zeta_1\Omega\left(\kappa-\lambda_0\Omega^2-\left(1+\frac{U^2}{2}\right)\lambda_1U^2\Omega^2\right)A_1=F_0^2, \tag{24b}$$

where A_1 and A_2 keep the original form shown by Eq. (17a) and (17b), respectively.

The backbone curves correspond to the relationship between the displacement amplitudes and the oscillation frequency of the unforced and undamped system, i.e., $\zeta_1=\zeta_2=0$ and $F_0=0$. For the current system, they can be obtained by solving the following two equations

$$(\gamma-\mu\Omega^2)^2R_1^2=\left(\gamma+\kappa-(\mu+\lambda_0)\Omega^2-\left(1+\frac{U^2}{2}\right)\lambda_1U^2\Omega^2\right)^2U^2, \tag{25a}$$

$$\left(1-(1+\lambda_0)\Omega^2-\left(1+\frac{R_1^2}{2}\right)\lambda_1R_1^2\Omega^2\right)^2R_1^2+\left(\kappa-\lambda_0\Omega^2-\left(1+\frac{U^2}{2}\right)\lambda_1U^2\Omega^2\right)^2U^2+2\left(1-(1+\lambda_0)\Omega^2-\left(1+\frac{R_1^2}{2}\right)\lambda_1R_1^2\Omega^2\right)\left(\kappa-\lambda_0\Omega^2-\left(1+\frac{U^2}{2}\right)\lambda_1U^2\Omega^2\right)A_2=0, \tag{25b}$$

where

$$A_2=\frac{(\gamma-\mu\Omega^2)}{\left(\gamma+\kappa-(\mu+\lambda_0)\Omega^2-\left(1+\frac{U^2}{2}\right)\lambda_1U^2\Omega^2\right)}R_1^2. \tag{26}$$

3.2. HB with Alternating-frequency-time scheme

To determine the steady-state responses of the system, Eq. (6) can also be solved by the harmonic balance (HB) method with alternating-frequency-time (AFT) technique [38]. The displacement response vector is approximated by a truncated N-th order Fourier series with a fundamental frequency of Ω:

$$\mathbf{X}=\left\{\sum_{n=0}^{N}\tilde{R}_{(1,n)}\exp(in\Omega\tau),\quad \sum_{n=0}^{N}\tilde{R}_{(2,n)}\exp(in\Omega\tau)\right\}^{\mathrm{T}}, \tag{27}$$

where $\tilde{R}_{(1,n)}$ and $\tilde{R}_{(2,n)}$ are the complex Fourier coefficients of the n-th order Fourier approximations associated with X_1 and X_2, respectively. By taking the differentiation of Eq. (27), the velocity and acceleration vectors can be obtained, and they are expressed as

$$\mathbf{X}'=\left\{\sum_{n=0}^{N}in\Omega\tilde{R}_{(1,n)}\exp(in\Omega\tau),\quad \sum_{n=0}^{N}in\Omega\tilde{R}_{(2,n)}\exp(in\Omega\tau)\right\}^{\mathrm{T}}, \tag{28a}$$

$$\mathbf{X}'' = \left\{-\sum_{n=0}^{N}(n\Omega)^2 \tilde{R}_{(1,n)} \exp(\mathrm{i}n\Omega\tau), \quad -\sum_{n=0}^{N}(n\Omega)^2 \tilde{R}_{(2,n)} \exp(\mathrm{i}n\Omega\tau)\right\}^{\mathrm{T}}, \tag{28b}$$

respectively. The nonlinear force vector generated by the inclusion of the nonlinear joints are

$$\mathbf{F_{nl}}(\mathbf{X}'', \mathbf{X}', \mathbf{X}) = \left\{\sum_{n=0}^{N} \widetilde{H}_{(1,n)} \exp(\mathrm{i}n\Omega\tau), \quad \sum_{n=0}^{N} \widetilde{H}_{(2,n)} \exp(\mathrm{i}n\Omega\tau)\right\}^{\mathrm{T}}, \tag{29}$$

where $\widetilde{H}_{(1,n)}$ and $\widetilde{H}_{(2,n)}$ are the complex Fourier coefficients of the n-th order associated with the nonlinear force terms $F_{\mathrm{bP}} + F_{\mathrm{bQ}}$ and $-F_{\mathrm{bP}}$, respectively. For the treatment of the nonlinear force, the AFT scheme is applied to determine the Fourier coefficient associated with a general nonlinear force, which may be smooth or non-smooth functions of the displacement, velocity or the acceleration [39]. The main idea of the AFT scheme is to replace the continuous Fourier transform of the nonlinear forces by a discrete Fourier transform so that samples of the nonlinear forces at equidistant time instants within one period of oscillation are taken.

By inserting Eqs. (27), (28) and (29) into Eq. (6) and balancing the coefficients of the n-th ($0 \leq n \leq N$) order harmonic term, we have

$$(-(n\Omega)^2\mathbf{M} + \mathrm{i}(n\Omega)\mathbf{C} + \mathbf{K})\widetilde{\mathbf{R}}_n = \tilde{\mathbf{S}}_n - \widetilde{\mathbf{H}}_n, \tag{30}$$

where $\widetilde{\mathbf{R}}_n = \left\{\tilde{R}_{(1,n)}, \quad \tilde{R}_{(2,n)}\right\}^{\mathrm{T}}$, $\widetilde{\mathbf{H}}_n = \left\{\widetilde{H}_{(1,n)}, \quad \widetilde{H}_{(2,n)}\right\}^{\mathrm{T}}$ and $\tilde{\mathbf{S}}_n = \{F_0, \quad 0\}^{\mathrm{T}}$. Note that Eq. (23) is an algebraic equation of complex numbers, and it can be transformed into two real algebraic equations. When the N-th order HB approximations are carried out, there will be a total number of 2(2N+1) real algebraic equations, which can be solved by Newton-Raphson method. To track the solution branches with variations of the system parameters or excitation parameters, the pseudo-arclength continuation methods is also used. Therefore, the steady-state response of the system can be determined and the effects of the nonlinear joints on the dynamics and the power flow behaviour of the coupled system can be determined.

To compare and verify the results obtained from different methods, Fig. 4(a) and (b) shows the steady-state displacement amplitudes $\lfloor X_1 \rfloor_{\max}$ and $\lfloor X_2 \rfloor_{\max}$ of masses m_1 and m_2, respectively. The system parameters are set as $\mu = 1, \gamma = 1, \kappa = 10, \zeta_1 = \zeta_2 = 0.01, F_0 = 0.05$ and the inerter-based nonlinear joint is added at position P. The solid line is for the system without adding inerter-based joint, i.e., $\lambda_0 = \lambda_1 = 0$. The HB-AFT results are based on 3rd order approximation and are denoted by the dashed line. The 1st HB results based on analytical derivations shown by Eq. (25), solved by a standard bisection method. The figure shows relatively good agreements of the results obtained from the three different approaches.

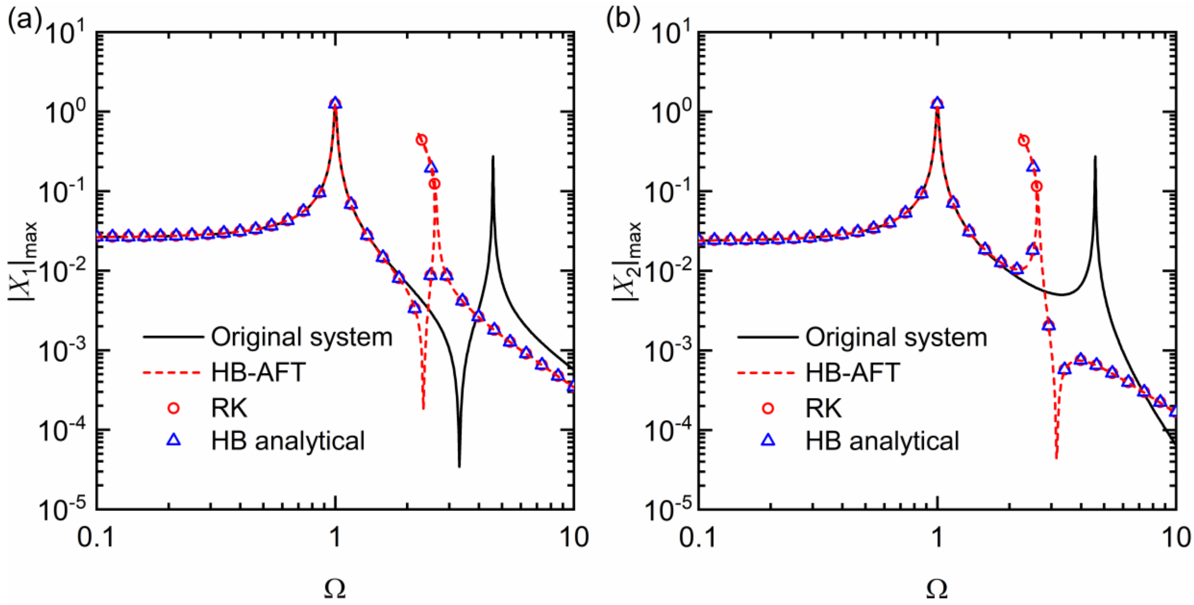

Fig. 4. Comparison of the response amplitudes obtained using different methods. Solid line: Dashed line: HB-AFT; Circles: RK results; Triangles: analytical HB.

4. Vibration transmission and energy flow

4.1. Force transmissibility

For vibration suppression of coupled systems, the vibration transmission between subsystems is of interest. In this study, the force transmission and vibration energy flow are both used to quantify the level of vibration transmission.

The force transmission *TR* from the primary system to the secondary system can be defined as the ratio between the magnitude of the force transmitted to S2 and that of the excitation force

$$TR = \frac{|F_T|}{F_0}, \tag{31}$$

where F_T represents the transmitted force to mass m_2 and is expressed by

$$F_T = \kappa(X_1 - X_2) + F_{\mathrm{bP}}. \tag{32}$$

4.2. Time-averaged energy flow and kinetic energies

4.2.1 Energy input

The dimensionless instantaneous input power into the system is the product of the excitation force and the velocity of mass m_1:

$$P_{\mathrm{in}} = \Re\{F_0 \exp(\mathrm{i}\Omega\tau + \mathrm{i}\phi)\}\Re\{X_1'\}, \tag{33}$$

where the symbol $\Re$ denotes the operation of taking the real part of a complex number. The time-averaged input power is

$$\overline{P}_{\mathrm{in}} = \frac{1}{\tau_{\mathrm{p}}}\int_{\tau_0}^{\tau_0+\tau_{\mathrm{p}}} P_{\mathrm{in}}\,\mathrm{d}\tau = 0.5F_0\Re\{\left(\mathrm{i}\Omega\tilde{R}_{(1,1)}\right)^*\} \approx 0.5F_0R_1\Omega\sin\phi, \tag{34}$$

where $X_1' = \sum_{n=0}^{N} \mathrm{i}n\Omega\tilde{R}_{(1,n)}\exp(\mathrm{i}n\Omega\tau)$ obtained from Eq. (21), τ_0 is the starting time for the averaging, τ_p is the averaging time span set as one cycle of the excitation with $\tau_\mathrm{p} = 2\pi/\Omega$, the symbol operator * denotes the operation of taking complex conjugate of a complex number, and Eq. (11a) has been used for the approximation .

4.2.2 Energy dissipation

The dimensionless instantaneous dissipated powers $P_{\mathrm{d}1}$ and $P_{\mathrm{d}2}$ by dampers c_1 and c_2 in S1 and S2 are obtained by taking the product of the damping forces and the corresponding relative velocities across the two ends of the dampers. The time-averaged dissipated powers are represented by

$$\overline{P}_{\mathrm{d}1} = \frac{1}{\tau_\mathrm{p}}\int_{\tau_0}^{\tau_0+\tau_\mathrm{p}} P_{\mathrm{d}1}\,\mathrm{d}\tau = \frac{1}{\tau_\mathrm{p}}\int_{\tau_0}^{\tau_0+\tau_\mathrm{p}} 2\zeta_1\left\{\Re\{X_1'\}\right\}^2 \mathrm{d}\tau \approx \zeta_1 R_1^2\Omega^2, \tag{35a}$$

$$\overline{P}_{\mathrm{d}2} = \frac{1}{\tau_\mathrm{p}}\int_{\tau_0}^{\tau_0+\tau_\mathrm{p}} P_{\mathrm{d}2}\,\mathrm{d}\tau = \frac{1}{\tau_\mathrm{p}}\int_{\tau_0}^{\tau_0+\tau_\mathrm{p}} 2\zeta_2\gamma\left\{\Re\{X_2'\}\right\}^2 \mathrm{d}\tau \approx \zeta_2\gamma R_2^2\Omega^2, \tag{35b}$$

where the first-order expressions of the velocities shown by Eq. (11a) and (b) have been used for the approximations. Note that over a cycle of a periodic response, the total mechanical energy remains unchanged, i.e., the total input energy by the excitation force should be fully dissipated by viscous dampers c_1 and c_2. Therefore, we have $\overline{P}_\mathrm{in} = \overline{P}_{\mathrm{d}1} + \overline{P}_{\mathrm{d}2}$.

4.2.3 Energy transmission

The dimensionless instantaneous time-averaged transmitted power to S2 is the product of the transmitted force and the corresponding velocity of mass m_2

$$P_\mathrm{t} = \Re\{F_\mathrm{T}\}\Re\{X_2'\}. \tag{36}$$

Time-averaged transmitted power is then obtained as

$$\overline{P}_\mathrm{t} = \frac{1}{\tau_\mathrm{p}}\int_{\tau_0}^{\tau_0+\tau_\mathrm{p}} P_\mathrm{t}\,\mathrm{d}\tau \approx \zeta_2\gamma R_2^2\Omega^2, \tag{37}$$

where that first-order expressions of the transmitted force F_T and velocity X_2' were used for the approximation. Note that for a periodic response, there is not net change in the total mechanical energy of subsystem S2 over a cycle of motion. Therefore, all the transmitted energy to S2 is dissipated by damper c_2. Consequently, we have $\overline{P}_\mathrm{t} = \overline{P}_{\mathrm{d}2}$. This behaviour was shown by first-order approximations shown by Eqs. (28b) and (30). The power transmission ratio R_t can be defined as the ratio between $\overline{P}_\mathrm{t}$ and $\overline{P}_\mathrm{in}$:

$$R_t = \frac{\overline{P}_\mathrm{t}}{\overline{P}_\mathrm{in}} = \frac{\overline{P}_{\mathrm{d}2}}{\overline{P}_{\mathrm{d}1}+\overline{P}_{\mathrm{d}2}}. \tag{38}$$

5. Results and discussions

In this section, the influence of adding the inerter-based nonlinear joint at two positions P and Q is investigated individually. Position P corresponds to the interface of the two subsystems S1 and S2, while position Q is placed within subsystem S1. The effects of the design parameters of lateral inerters and axial inerters are analysed, respectively. With a balanced consideration of the accuracy of the results and the computational efforts, the HB-AFT method with order $N = 3$ is used to obtain the displacement response, force transmissibility, and time-averaged power flow variables. The values of the system parameters and the excitation are selected as $\mu = 1, \gamma = 1, \kappa = 10, \zeta_1 = \zeta_2 = 0.01, F_0 = 0.05$. The HB-AFT results are presented by different types of lines and are compared with those obtained by the fourth order RK method denoted by different kinds of symbols.

5.1 Inerter-based joint added to position P ($F_{\mathrm{bQ}} = 0$)

5.1.1. Effects of the lateral inerters

Here the inclusion of the inerter-based nonlinear joint to position P at the coupling interface of the subsystems is considered. Figs. 5. 6 and 7 show the effects of the parameters of the lateral inerters on the steady-state displacement response, the time-averaged input and transmitted powers, as well as the force transmissibility and power transmission ratio, respectively. Case one is for the system without adding the nonlinear joint by setting the inertance of both the axial and the lateral inerters to be $\lambda_0 = \lambda_1 = 0$. The effects of the lateral inerters are investigated by changing their inertance λ_1 from 0, to 1 and then to 5 in Cases two, three and four, respectively, while fixing the inertance of the axial inerter as $\lambda_0 = 1$. The HB-AFT results for Cases one, two, three and four are represented by the solid, dashed, dash-dotted and dotted lines, respectively.

Figure 5(a) and (b) shows the influence of the lateral inerters on the steady-state displacement response amplitude $\lfloor X_1 \rfloor_{\max}$ of mass m_1 and the relative displacement amplitude $\lfloor X_2 - X_1 \rfloor_{\max}$ between the masses. Fig. 5(a) shows that for the original coupled system without adding the nonlinear joint, there are two resonant peaks in the curve of $\lfloor X_1 \rfloor_{\max}$. After adding a joint with only the axial inerter with an inertance-to-mass ratio of $\lambda_0 = 1$, the second peak of $\lfloor X_1 \rfloor_{\max}$ moves to the left and the corresponding peak value is increased. However, the first peak frequency and value of $\lfloor X_1 \rfloor_{\max}$ remain nearly unchanged in spite of the variations in λ_0 and λ_1 for the four cases. There is an anti-peak in each curve of $\lfloor X_1 \rfloor_{\max}$, which shifts to low-frequency range with the addition of the axial inerter λ_0. This anti-peak remains almost the same regardless of the changes in the inertance λ_1 of the lateral inerters in Cases two, three and four. The reason for the effects is that when the response amplitude is large, the nonlinearity introduced by the lateral inerters as shown by the nonlinear force term becomes stronger. In contrast, when the response amplitude is low, as is the case at the anti-peak, the response amplitude is small such as the nonlinear force term is small, leading to a negligible effect of the changing inertance of the lateral inerters on the response. Fig. 5(a) also shows that the displacement amplitude $\lfloor X_1 \rfloor_{\max}$ at the second peak frequency of mass m_1 is reduced by adding the nonlinear joint in Cases three and four, compared to Case two. This behaviour demonstrates that the inerter-based nonlinear joint can be used to suppress the vibration at prescribed excitation frequencies. Fig. 5(b) shows that only one peak exists in each curve of the relative displacement amplitude $\lfloor X_1 - X_2 \rfloor_{\max}$, corresponding to the out-of-phase mode of the system. It is found that the addition of the axial inerter can move this peak to lower frequency range. This peak bends to the left with the addition of lateral inerters. An increase in the value of λ_1 from 0, to 1 and then to 5 for the lateral inerters can further twist the peak to low-frequency range with slight increases in the peak value.

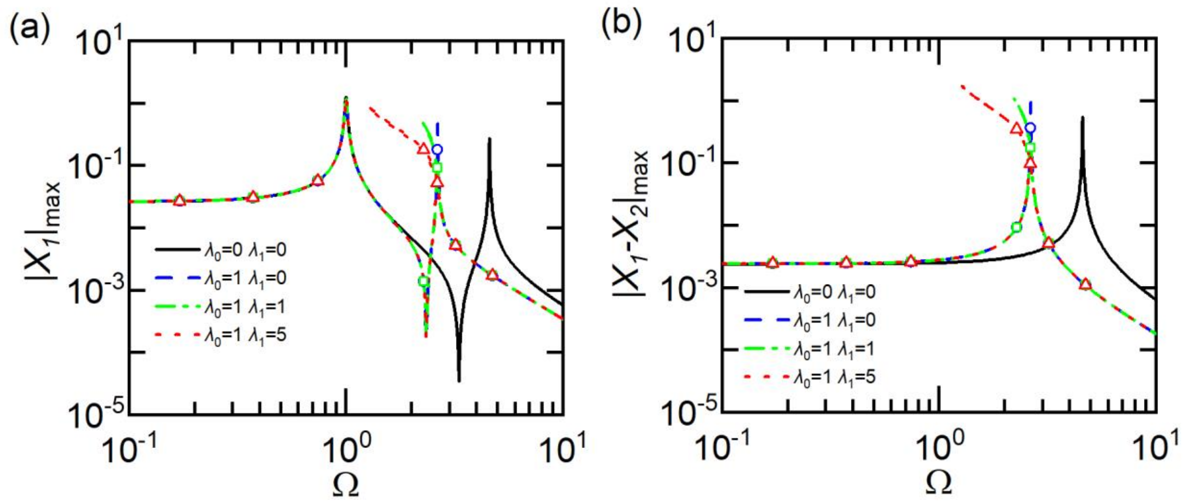

Fig. 5. Effects of the inerter-based nonlinear joint on (a) the response amplitude of mass m_1, and (b) the relative response of masses m_1 and m_2 when the inerter-based joint is added at P ($\mu = 1, \gamma = 1, \varkappa = 10, \zeta_1 = \zeta_2 = 0.01, F_0 = 0.05$).

As shown in Fig. 6 (a) and (b), the time-averaged input power $\bar{P}_{\mathrm{in}}$ and transmitted power $\bar{P}_{\mathrm{t}}$ are examined. Fig. 6(a) shows two peaks in each curve of $\bar{P}_{\mathrm{in}}$. It is shown that with the addition of axial inerter $\lambda_0 = 1$ from Case one to Case two, the second peak of time-averaged input power moves to lower frequency range from $\Omega \approx 4.6$ to $\Omega \approx 2.6$. This peak further bends towards the low frequencies as λ_1 increases from 0 to 1, and to 5, from Cases two to three and four. There are slight changes in the second peak value of $\bar{P}_{\mathrm{in}}$ with the changes in λ_0 and λ_1. However, the first peak value and peak frequency obtained at $\Omega \approx 1$ remain almost the same regardless of the changes in λ_0 and λ_1 in the four cases considered. Fig. 6(a) shows that the time-averaged power into the system is mainly affected by the lateral inerters at the coupling interface when the excitation frequency is in the vicinity of the second resonance peak. The addition of inerter-based nonlinear joint reduces the time-averaged input power when $\Omega > 3.2$ and the effects of the nonlinear joint are relatively small at low excitation frequencies with $\Omega < 2$. Fig. 6(b) shows that an anti-peak of time-averaged transmitted power $\bar{P}_{\mathrm{t}}$ is introduced by the addition of the axial inerter at the interface of the coupled system. The second peak of the transmitted power moves to lower frequencies after introducing the linear inerter at position P. It is further bent to the lower frequency range with the involvement of lateral inerters. This phenomenon indicates that a large value of inertance λ_0 and λ_1 leads to higher amount of vibration power transmission from subsystem one to subsystem two from $\Omega \approx 1.9$ to $\Omega \approx 2.8$ and also in the high-frequency range $\Omega > 7.1$. A reduction of power transmission is noticed between $2.8 < \Omega < 7.1$ in Fig. 6(b), especially in the vicinity of the anti-peak obtained at $\Omega \approx 3.2$. This figure suggests that the vibration transmission can be effectively reduced at prescribed excitation frequencies. The value of the inerter-based nonlinear joint can be further tailored for the suppression of vibration transmission based on the excitation frequency.

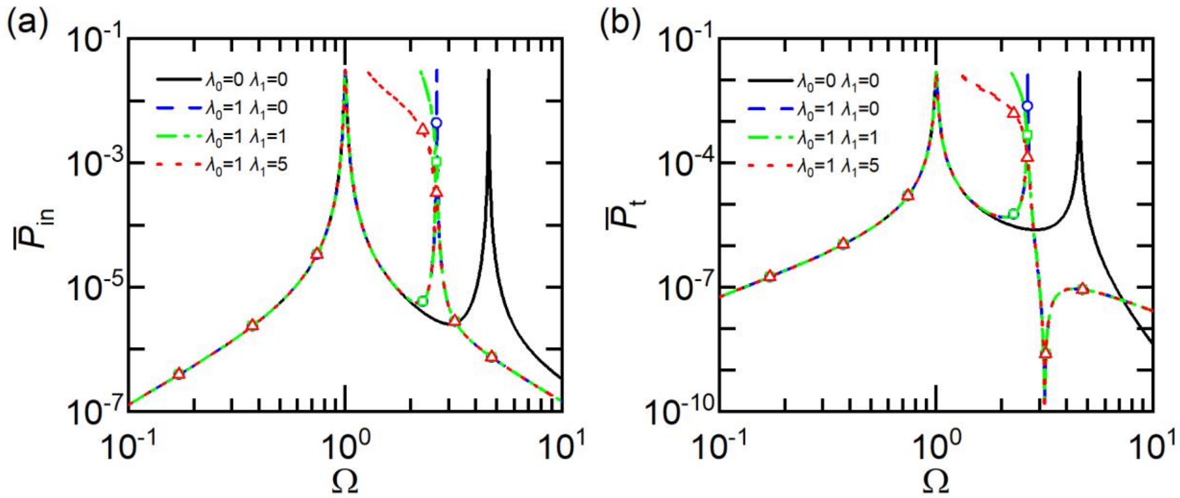

Fig. 6. Effects of the inerter-based nonlinear joint on (a) the time-averaged input power $\bar{P}_{\text{in}}$, and (b) the time-averaged transmitted power $\bar{P}_{\text{t}}$ when the inerter-based joint is added at P ($\mu = 1, \gamma = 1, \varkappa = 10, \zeta_1 = \zeta_2 = 0.01, F_0 = 0.05$).

Figure 7(a) and (b) illustrates the influence of adding the inerter-based joint at the interface of the coupled system on the force transmissibility and power transmission ratio from subsystem one to subsystem two. In Fig. 7(a), it is observed that the addition of the linear inerter at the interface of the coupled system causes the resonance peak of force transmissibility to shift to a lower frequency range. An anti-peak is introduced at $\Omega \approx 3.2$ around where the force transmissibility is greatly reduced. The peak bends towards lower frequencies when the nonlinear inerter is further included. Fig. 7(a) shows that the effect of inerter is negligible at low frequencies with $\Omega < 1.5$. The force transmission from subsystem one to subsystem two is increased with the inclusion of the axial inerter in the joint device from $\Omega \approx 1.3$ to $\Omega \approx 2.8$ for Case four, and gretly reduced from $\Omega \approx 2.8$ to $\Omega \approx 7.2$. This character suggests that the force transmission can be effectively reduced in prescribed excitation frequency range. In Fig. 7(b), the influence of the inerter-based nonlinear joint on the power transmission ratio R_t from subsystem one to subsystem two is examined. It is shown that the inclusion of the linear inerter shifts the original peak of R_t from $\Omega \approx 3.3$ to $\Omega \approx 2.3$ with the similar peak height. An anti-peak is introduced at $\Omega \approx 3.2$ resulted from the anti-peak introduced in the time-averaged transmitted power $\bar{P}_{\text{t}}$ at this frequency. A fluctuation of power transmission ratio is observed within $1.3 < \Omega < 2.7$ when the lateral inerters are further included. As shown in the enlarged view in Fig. 7(b), compared with Case two with only the axial inerter $\lambda_0 = 1$, the nonlinear joint in Cases three and four with $\lambda_1 = 1$ and 5 introduces a horizontal notch in the curve of R_t. A larger nonlinear inertance value λ_1 of the lateral inerter leads to a wider horizontal notch of the power transmission ratio R_t. When the excitation frequency is relatively small, i.e., $\Omega < 1.3$, the impact of the inerter-based nonlinear joint tends to be small. The power transmission ratio is increased at high frequencies $\Omega > 5.8$ with the inclusion of the joint device in Cases two, three and four, compared with Case one. This phenomenon indicates that the power transmission ratio of the coupled system can be highly reduced at prescribed frequencies.

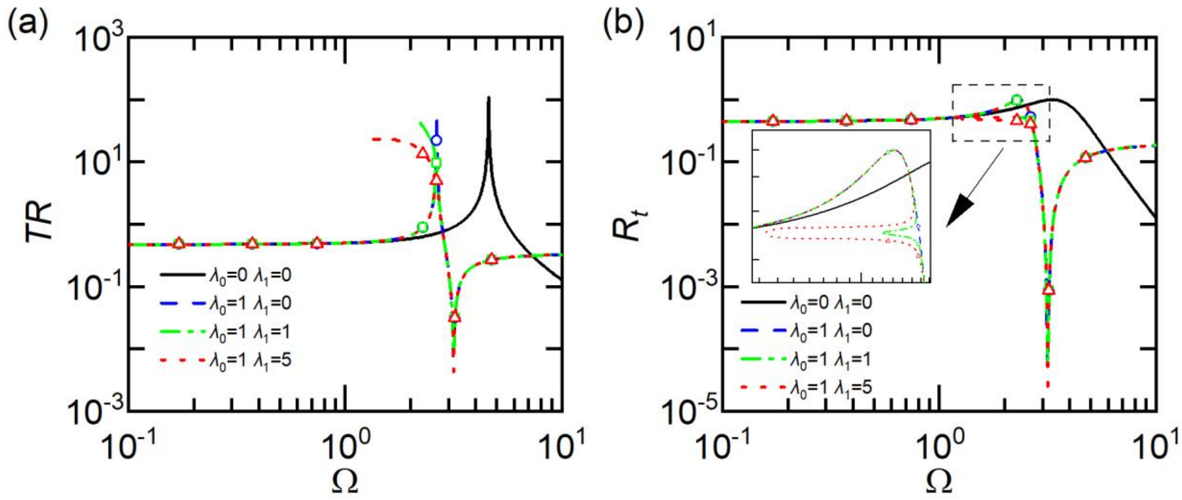

Fig. 7. Effects of the inerter-based nonlinear joint on (a) the force transmissibility TR, and (b) the time-averaged power transmission ratio R_t when the inerter-based joint is added at P ($\mu = 1, \gamma = 1, \varkappa = 10, \zeta_1 = \zeta_2 = 0.01, F_0 = 0.05$).

5.1.2. Effects of the axial inerter

In this section, the influence of the axial inerter is investigated. The inerter-based nonlinear joint is added at position P. Figs. 8, 9 and 10 show the effects of the parameters of the axial inerter on the steady-state response, the time-averaged power flow as well as the force transmissibility and power transmission ratio of the system. There are four cases considered and the HB-AFT results are shown by different curves. Case one with $\lambda_0 = \lambda_1 = 0$ refers to the original system without adding the joint and the results are presented by solid lines. In Cases two, three and four, a nonlinear joint with different inertance of the axial inerter is added at position P setting $\lambda_0 = 1, 5$ and 10, respectively, while fixing $\lambda_1 = 2$. The HB-AFT results for Cases two, three and four are shown by the dashed, dash-dotted, and dotted lines, respectively, while the corresponding RK results are shown by circles, squares and triangles.

In Fig. 8, effects of the axial inerter on the maximum steady-state displacement response $|X_1|_{\max}$ of the primary mass m_1 and the amplitude of the relative displacement $|X_1 - X_2|_{\max}$ between the masses m_1 and m_2 are investigated. Fig. 8(a) shows two peaks in the curve of Case one. The addition of a nonlinear joint at position P in Cases two, three and four shifts the second peak of $|X_1|_{\max}$ to lower frequencies. By the increase in λ_0 from 1, to 5 and then to 10, the second peak and the anti-peak in each curve of $|X_1|_{\max}$ both move to the low-frequency range with larger second peak value and also the value at the anti-peak. It is noted that with the increase in the value of λ_0, there is less bending in the second peak of $|X_1|_{\max}$ suggesting that the nonlinearity becomes weaker. In Case four, with the inertance-to-mass ratio of the axial inerter increases to $\lambda_0 = 10$, the second peak corresponding to the out-of-phase mode of $|X_1|_{\max}$ tends to merge with the first peak, which is associated with the in-phase mode. It is also shown that the bending out-of-phase peak is slightly higher than the in-phase peak when $\lambda_0 = 10, \lambda_1 = 2$. The effects of the changes in λ_0 of the inerter-based nonlinear joint on the value of $|X_1|_{\max}$ is negligible in the low-frequency range with $\Omega < 0.96$. Fig. 8(b) shows the influence of the variations in the inertance λ_0 of the inerter-based joint on the relative displacement of two masses m_1 and m_2. It is observed that with the increase of the inertance λ_0 of the axial inerter from 1 to 5 and then 10, the peak frequency of $|X_1 - X_2|_{\max}$ is reduced but the peak value increases. From Case two to Case four, there is less bending of the peak, suggesting that the nonlinear inertial effect brought by the addition of the nonlinear joint becomes weaker. Comparing Case four with Case one, Fig. 8(b) shows that the increase in λ_0 results in a reduction of relative displacement at high frequencies with $\Omega > 1.4$. There is an increase in $|X_1 - X_2|_{\max}$ when the excitation frequency is between $0.4 < \Omega < 1.4$. This inerter-based joint has weaker influence on $|X_1 - X_2|_{\max}$ at low frequencies with $\Omega < 0.4$.

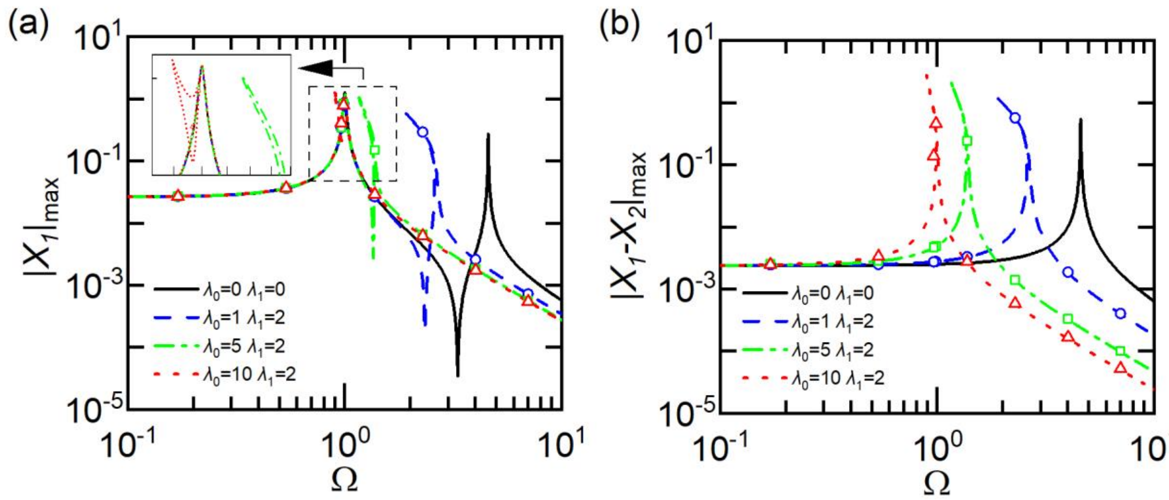

Fig. 8. Effects of the inerter-based nonlinear joint on (a) the response amplitude of mass m_1, and (b) the relative response of masses m_1 and m_2 when the inerter-based joint is added at P ($\mu = 1, \gamma = 1, \varkappa = 10, \zeta_1 = \zeta_2 = 0.01, F_0 = 0.05$).

Figure 9(a) and (b) shows the effects of the inertance-to-mass ratios λ_0 and λ_1 of the inerter-based joint on the time-averaged input power $\bar{P}_{\rm in}$ and the time-averaged transmitted power $\bar{P}_{\rm t}$ to the secondary mass m_2, respectively. Fig. 9(a) shows that the lateral inerters bend the second peak of $\bar{P}_{\rm in}$ to low-frequency range. With the increase in λ_0 from 1, to 5 and then to 10 for the axial inerter, this peak is shifted to the low-frequency range. The corresponding peak height remains almost the same with the increase of λ_0 from Case two to Case four. The other peak associated with the in-phase mode remains to be approximately at the same frequency and of the same value regardless of the changes in λ_0 and λ_1. In Case four with $\lambda_0 = 10$ for the axial inerter, the bending peak merges with the corresponding peak associated with the in-phase mode. Also, for this case, the corresponding peak value of $\bar{P}_{\rm in}$ for the out-of-phase mode becomes smaller than the peak associated with in-phase mode. It is observed that with the increase of λ_0 from Case two to Case four, there is less extent of the bending. Fig. 9(b) shows that the second peak of the time-averaged transmitted power bends towards low frequencies by the addition of the inerter-based nonlinear joint at position P. The inclusion of the joint in Case two introduces an anti-peak of $\bar{P}_{\mathrm{t}}$ at $\Omega \approx 3.17$. Both the out-of-phase mode peak and the anti-peak move to lower frequency range with the increase of axial inertance λ_0 from Case two to Case four. In Case four with $\lambda_0 = 10$, the out-of-phase peak merges with the in-phase peak as well as the anti-peak. As shown in the enlarged view in Fig. 9(b), the peak value of the in-phase mode peak is not reduced, while the out-of-phase mode peak is slightly reduced compared with Case one. Comparing Case four with Case one, an increase of power transmission to subsystem two is noticed at high frequencies Ω >7 and the effect of inerter-based nonlinear joint becomes small at low frequencies. From the viewpoint of power transmission, the level of vibration transmission to subsystem S2 is greatly reduced within $1.5 < \Omega < 7$ by the using nonlinear joint in Case four.

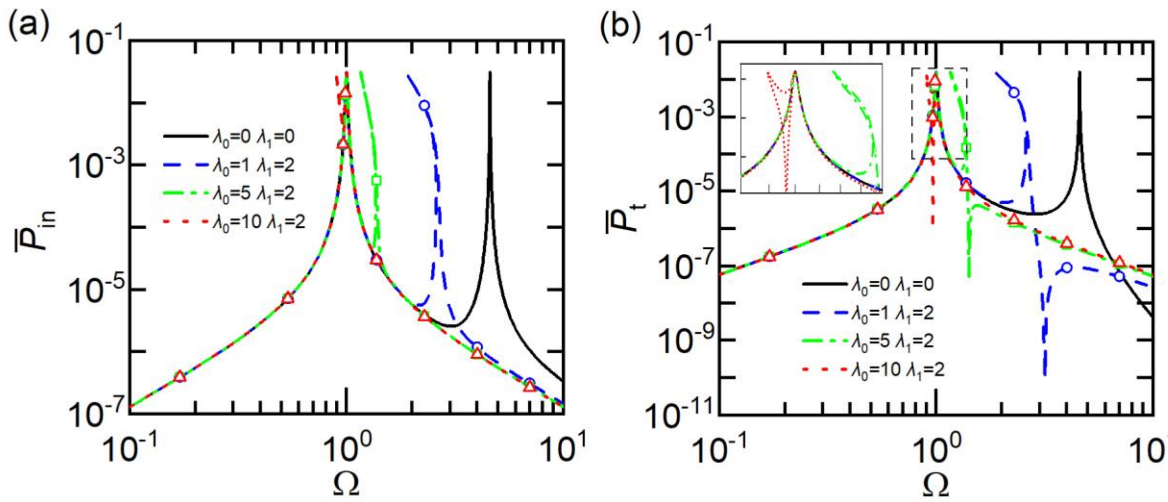

Fig. 9. Effects of the inerter-based nonlinear joint on (a) the time-averaged input power $\bar{P}_{\mathrm{in}}$, and (b) the time-averaged transmitted power $\bar{P}_{\mathrm{t}}$ when the inerter-based joint is added at P ($\mu = 1, \gamma = 1, \varkappa = 10, \zeta_1 = \zeta_2 = 0.01, F_0 = 0.05$).

Figure 10(a) and (b) shows the effects of the inerter-based nonlinear joint on the force transmissibility TR and power transmission ratio R_t within the system, respectively. Fig. 10(a) shows only one peak in each curve of TR, corresponding to the out-of-phase mode of the system. Compared with Case one, the addition of the inerter-based nonlinear joint in Case two twists the peak of force transmissibility to lower frequencies. The increase of the inertance λ_0 of the axial inerter shifts this peak to lower frequency range and correspondingly reduces the peak value. However, the corresponding bending effect due to the nonlinearity of lateral inerters becomes smaller with the increase of λ_0. An anti-peak of force transmissibility is introduced by adding the inerter-based joint in Cases two, three and four. The peak value of TR is reduced after increasing the value of axial inertance λ_0 from 1 to 10. The anti-peak almost disappears when the inertance λ_0 of the axial inerter increases to 10. The figure shows that the level of force transmission to mass m_2 can be reduced at the original peak frequency of Case one, i.e., the original system without adding the joint. However, there might be larger force transmission at high excitation frequencies. Fig. 10(b) shows that compared with Case one an anti-peak exits in each curve of the power transmission ratio in Cases two, three and four. A horizontal fluctuation appears at $R_t \approx 0.45$ due to the addition of lateral inerters. This fluctuation becomes smaller as the inertance of the axial inerter increases. The figure also shows that the inclusion of the inerter-based joint increases the power transmission ratio at high frequencies. A larger value of the inertance λ_0 leads to a higher value of power transmission ratio R_t in the high-frequency range. The figure shows that both TR and R_t both tend to asymptotic values when the excitation frequency Ω increases in the high-frequency range. The effects of adding the inerter-based nonlinear joint on force transmissibility and the power transmission ratio becomes weaker at low excitation frequencies.

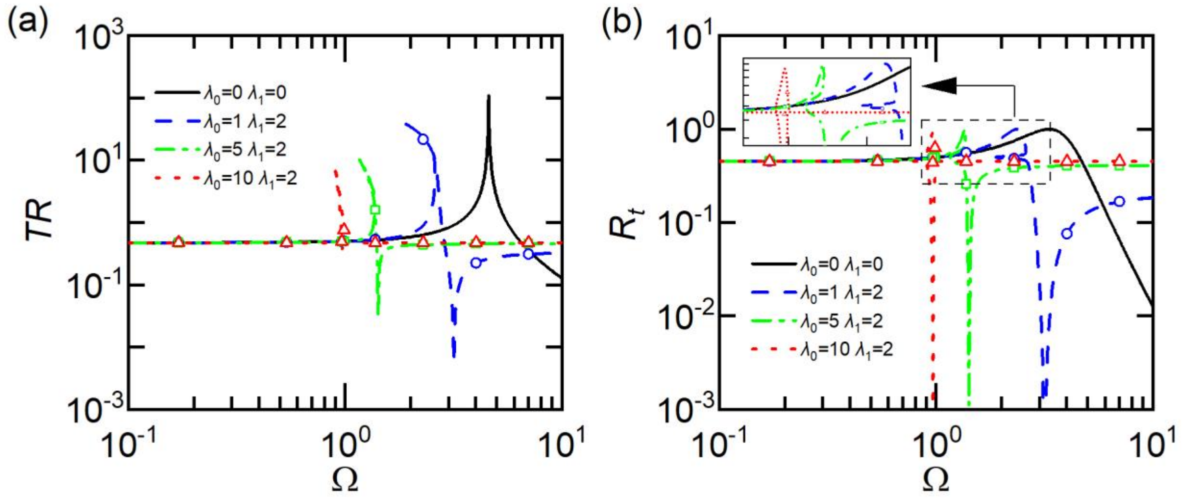

Fig. 10. Effects of the inerter-based nonlinear joint on (a) the force transmissibility T_R, and (b) the time-averaged power transmission ratio R_t when the inerter-based joint is added at P ($\mu = 1, \gamma = 1, \varkappa = 10, \zeta_1 = \zeta_2 = 0.01, F_0 = 0.05$).

5.2. Nonlinear Inerter added to position Q ($F_{\mathrm{bP}} = 0$)

5.2.1. Effects of the lateral inerters

Here the effects of the lateral inerters in the inerter-based nonlinear joint at position Q on the steady-state response, time-averaged input and transmitted powers, force transmissibility, and the power transmission ratio are investigated. Four cases are considered with Case one for the original system without adding the inerter-based joint (i.e., $\lambda_0 = \lambda_1 = 0$) and the analytical results are represented by solid lines. In Cases two, only the axial inerter exits in the joint device by setting $\lambda_0 = 1$ and $\lambda_1 = 0$ and the analytical results are shown by dashed lines. In Cases three and four, the inertance λ_1 of the lateral inerters is selected as $\lambda_1 = 1$ and $\lambda_1 = 5$, while fixing $\lambda_0 = 1$, which are represented by dash-dotted and dotted lines, respectively.

Figure 11(a) shows that there are two resonance peaks and one anti-peak in each curve of the steady-state response amplitude of displacement $|X_1|_{\max}$. A comparison of Cases one and two shows that by the addition of the joint comprising only the axial inerter with $\lambda_0 = 1$, both peaks of $|X_1|_{\max}$ shift to the low-frequency range. The height of the first peak is slightly increased, while the second one reduces. However, for both cases, an anti-peak is obtained at $\Omega \approx 3.3$ and the corresponding value of $|X_1|_{\max}$

remains almost the same. The first peak bends towards lower frequency range with the further inclusion of lateral inerters in Case three and four. Comparing Case three with Case four, it shows that a larger value of λ_1 of the lateral inerters can bend the first peak further to the low-frequency range, and the corresponding peak value becomes larger. However, the second peak as well as the anti-peak change little despite of the variations in the values of λ_1 in the inerter-based nonlinear joint compared with Case one. It is observed that the effect of adding the inerter-based joint is negligible at low frequencies with $\Omega < 3.4$. Compared with Case one, the response amplitude $|X_1|_{\max}$ associated with the other three cases is reduced at high frequencies $\Omega > 4.2$. Fig. 11(b) shows the variations of the relative displacement amplitude $|X_1 - X_2|_{\max}$ of two masses m_1 and m_2. It shows that the use of the axial inerter results in another peak in the low-frequency range and also an anti-peak between the two peaks. Detailed analysis of the time histories shows that the peak in low-frequency range corresponds to an in-phase mode, while the one found at a higher frequency corresponds to an out-of-phase mode. This property is investigated in more details in Fig. 12 by examining the time histories of the steady-state displacement responses.

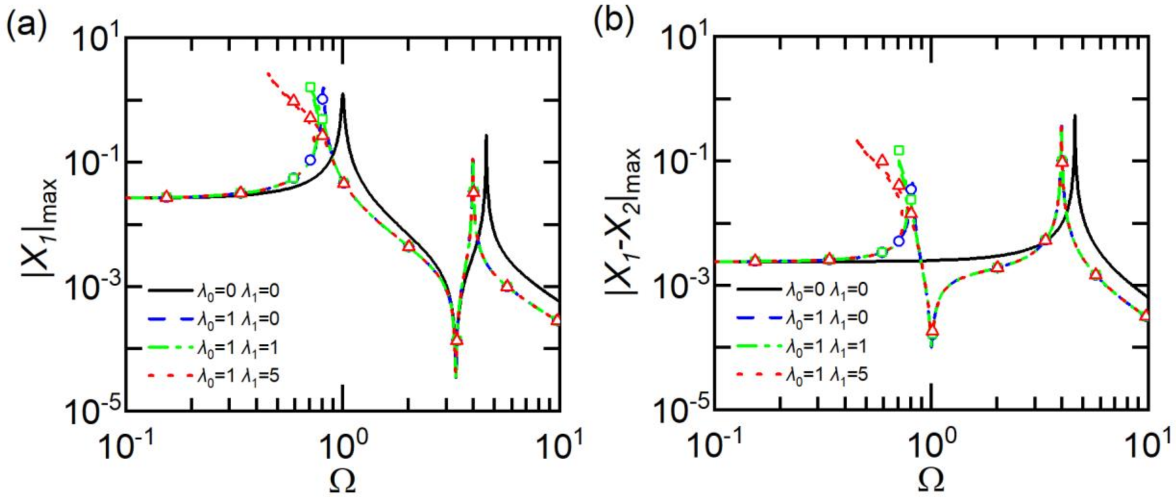

Fig. 11. Effects of the inerter-based nonlinear joint on (a) the response amplitude of mass m_1, and (b) the relative response of masses m_1 and m_2 when the inerter-based joint is added at Q ($\mu = 1, \gamma = 1, \varkappa = 10, \zeta_1 = \zeta_2 = 0.01, F_0 = 0.05$).

Figure 12(a) and (b) presents the time histories of the dimensionless steady-state displacements $|X_1|$ and $|X_2|$ to reveal the reason for the presence of an extra peak in $|X_1 - X_2|_{\max}$ by the addition of the inerter-based joint for Case two. Fig. 12(a) shows that two displacement curves reach their maximum value and minimum value at the same time, which indicates that the first peak in Fig. 11(a) and (b) corresponds to an in-phase mode. On the contrary, in Fig. 12(b) with $\Omega = 3.98$, when $|X_1|$ reaches its maximum value, $|X_2|$ is at its minimum, suggesting that the second peak in Fig. 11(a) and (b) correspond to an out-of-phase mode. It is recalled that the influence of the inerter-based nonlinear on the first peak (in-phase-mode) is stronger than that on the second peak (out-of-phase mode) in Fig. 11(a). This behaviour arises from the fact that the inerter-based nonlinear joint is now added to position Q.

The nonlinearity and also the nonlinear inertance force depend on the response of the first mass only. As shown in Fig. 12, the displacement amplitude of mass m_1 at $\Omega = 0.81$ is much larger than the one at $\Omega = 3.98$. Consequently, there is a stronger effect introduced by the nonlinearity of the joint device at the first peak.

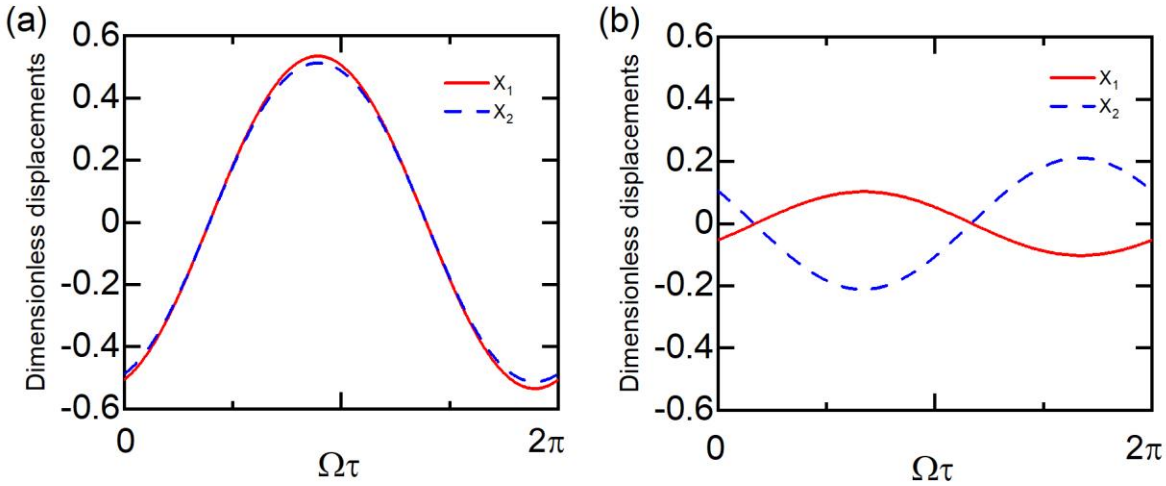

Fig. 12. Time histories of the steady-state dimensionless displacement response $|X_1|$ and $|X_2|$ with excitation at (a) $\Omega = 0.81$, and (b) $\Omega = 3.98$ ($\mu = 1, \gamma = 1, \varkappa = 10, \zeta_1 = \zeta_2 = 0.01, F_0 = 0.05, \lambda_0 = 1, \lambda_1 = 1$).

In Fig. 13(a) and (b), the influence of adding the inerter-based joint to point Q on the time-averaged input power $\bar{P}_{\mathrm{in}}$ and transmitted power $\bar{P}_{\mathrm{t}}$ is examined. It shows that two peaks are observed in each curve $\bar{P}_{\mathrm{in}}$ and $\bar{P}_{\mathrm{t}}$. Compared with Case one, the inclusion of the axial inerter in the joint device shifts both peaks in each curve to lower frequency range. The second peak in Case two reduces slightly after connecting the linear inerter at position Q compared with Case one, while the height of the first peak remains almost the same despite of changes in λ_0 and λ_1. By adding the lateral inerters in Case three, the first peak corresponding to the in-phase mode bends to lower frequency range. A higher inertance of the lateral inerter with $\lambda_1 = 5$ in Case four bends the first peak to further lower frequency range. The addition of the inerter-based nonlinear joint has much weaker influence when the excitation frequency is small. The figure shows that by adding the inerter-based joint to the system as in Cases two, three and our, there is less amount of the time-averaged input and transmitted power at high excitation frequencies. Note that the second peak in Case one reduces slightly after connecting the linear inerter at position Q, while the height of the first peak remains almost the same despite of changes in λ_0 and λ_1, suggesting the potential benefits of the inerter-based joint in vibration suppression in terms of vibration energy transmission within the system.

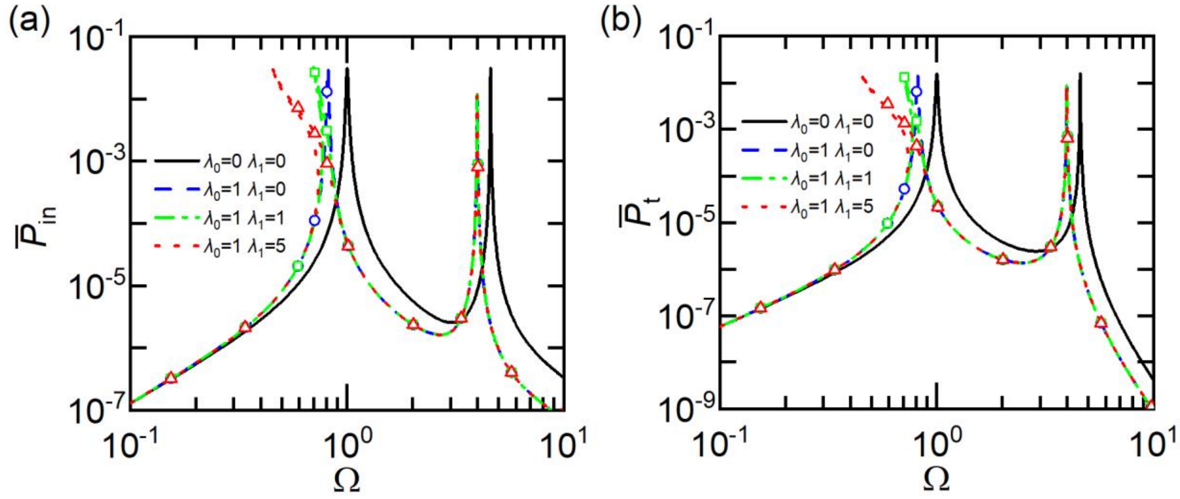

Fig. 13. Effects of the inerter-based nonlinear joint on (a) the time-averaged input power $\bar{P}_{\mathrm{in}}$, and (b) the time-averaged transmitted power $\bar{P}_{\mathrm{t}}$ when the inerter-based joint is added at Q ($\mu = 1, \gamma = 1, \varkappa = 10, \zeta_1 = \zeta_2 = 0.01, F_0 = 0.05$).

Figure 14(a) and (b) shows the influence of the inerter-based joint at point Q on the force transmissibility TR and the power transmission ratio R_{t}, respectively. Fig. 14(a) shows that for the original system without the inerter-based joint as in Case one, only one peak is observed in the curve of TR. The inclusion of the inerter-based joint with only the axial inerter in Case two reduces this peak value and the peak frequency, which is beneficial for suppression of vibration transmission. Another peak in the curve of TR is introduced at a lower value of the excitation frequency, the value of which is smaller than the second peak value. An anti-peak is generated between these two peaks at $\Omega \approx 1$, which can be used to substantially reduce vibration force transmissibility. In Case three with the addition of the lateral inerters in the joint, the first peak of TR bends towards low frequencies with slightly larger peak value. In Case four, the value of λ_1 is further increased to 5, which leads to the further bending of the first peak in TR to the left with a higher peak value. However, the second peak and the anti-peak in each curve of TR keep almost the same for Cases two, three and four regardless the variations in λ_1. Fig. 14(b) shows a peak in each cure of the power transmission ratio R_t. It shows that the power transmission is not sensitive to the changes in the values of λ_0 and λ_1 for the four cases considered. Detailed explanations and mathematical derivations are shown in the Appendix.

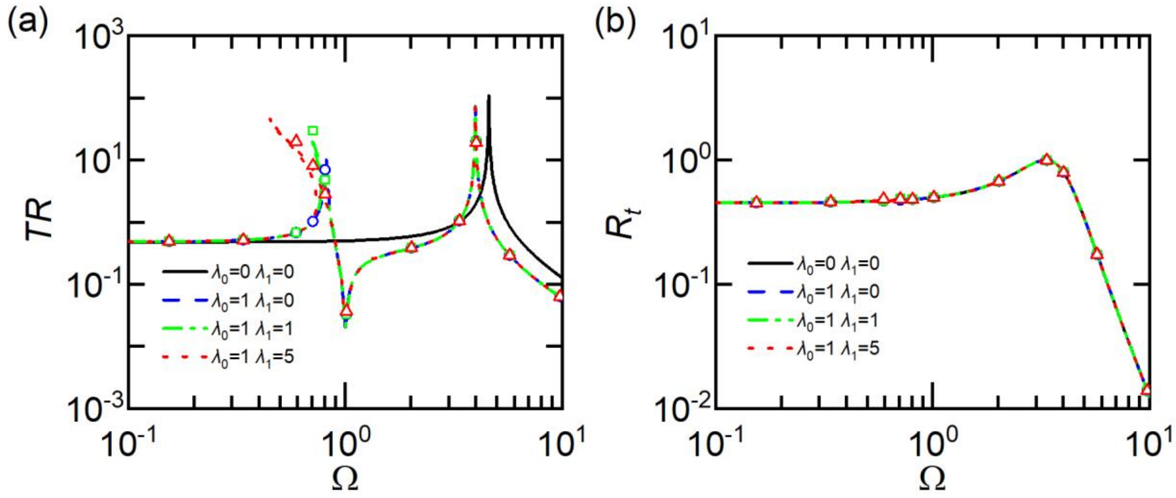

Fig. 14. Effects of the inerter-based nonlinear joint on (a) the force transmissibility TR, and (b) the time-averaged power transmission ratio R_t when the inerter-based joint is added at Q ($\mu = 1, \gamma = 1, \varkappa = 10, \zeta_1 = \zeta_2 = 0.01, F_0 = 0.05$).

5.2.2. Effects of the axial inerter

Here the effects of the axial inerter in the inerter-based nonlinear joint added to position Q with subsystem S1 are investigated. Figs. 15, 16 and17 show the variations of the steady-state response, the time-averaged power flow, force transmissibility, and power transmission of the system. Four cases are considered in each figure, which are obtained by HB-AFT method and verified by RK method. The solid line represents the results from Case one considering the system without adding inerter-based joint, i.e., $\lambda_0 = \lambda_1 = 0$. To examine the effect of the axial inerter, the value of λ_0 changes from 1, to 5 and then to 10 in Cases two, three and four, respectively, while setting the inertance of the lateral inerters $\lambda_1 = 2$. The corresponding HB-AFT results are plotted by the dashed, dash-dotted, and dotted lines, respectively.

Figure 15 demonstrates the effects of the inerter-based nonlinear joint added at position Q on the displacement response amplitude $|X_1|_{\max}$ of the primary mass and the relative displacement response amplitude $|X_1 - X_2|_{\max}$ of two masses. Fig. 15(a) shows that two peaks exist in each curve of $|X_1|_{\max}$. The inclusion of nonlinear inerter-based joint with $\lambda_0 = 1$ and $\lambda_1 = 2$ in Case two shifts the first peak to lower frequencies and bend it towards the left. Examinations of Cases two, three and four shows that increases of the inertance λ_0 from 1 to 5 then to 10 shift the first peak to lower frequencies and the corresponding peak value increases. As the inertance of the lateral inerters are fixed, the extent of bending of the first peak reduces from Case two to Case four. The second peak of $|X_1|_{\max}$ found at a relatively higher frequency also shifts to the left with the increase of λ_0, and the corresponding peak value reduces. In comparison, the frequency where the anti-peak is found on each curve remains almost the same regardless of the variations in the inertance-to-mass ratios λ_0 and λ_1. Compared with Case one, the addition of the inerter-based joint in Case two can reduce the response amplitude of the mass m_1 at prescribed frequencies, especially at high frequencies with $\Omega > 4.2$ and near the original peak frequency of $\Omega \approx 1$. This behaviour shows the benefits of using the inerter-based joint on vibration suppression. The effects of adding the joint device on the dynamic response becomes weak at low excitation frequencies with $\Omega < 0.14$. Fig. 15(b) shows that for the original system without the inerter-based joint (i.e., Case one), only one peak exists in the curve of the relative displacement amplitude. In contrast, for Cases two, three and four, there are two peaks in each curve of $|X_1 - X_2|_{\max}$ and an anti-peak is found between the two peaks. The first peak found at low frequencies bends towards the left while there is no noticeable bending for the second peak. For a fixed value of $\lambda_1 = 2$ for the lateral inerters, an increase of inertance λ_0 for the axial inerter shifts both peaks to the low-frequency range, while the anti-peak is found at approximately the same frequency. With the increase in λ_0 from Case two to Cases three and four, the first peak corresponding to the in-phase mode becomes higher, while the second peak becomes lower. As the excitation frequency reduces to the range where $\Omega < 0.14$, the curves associated with the four cases tend to merge, suggesting that the addition of the inerter-based joint has less impact on the relative displacement amplitude.

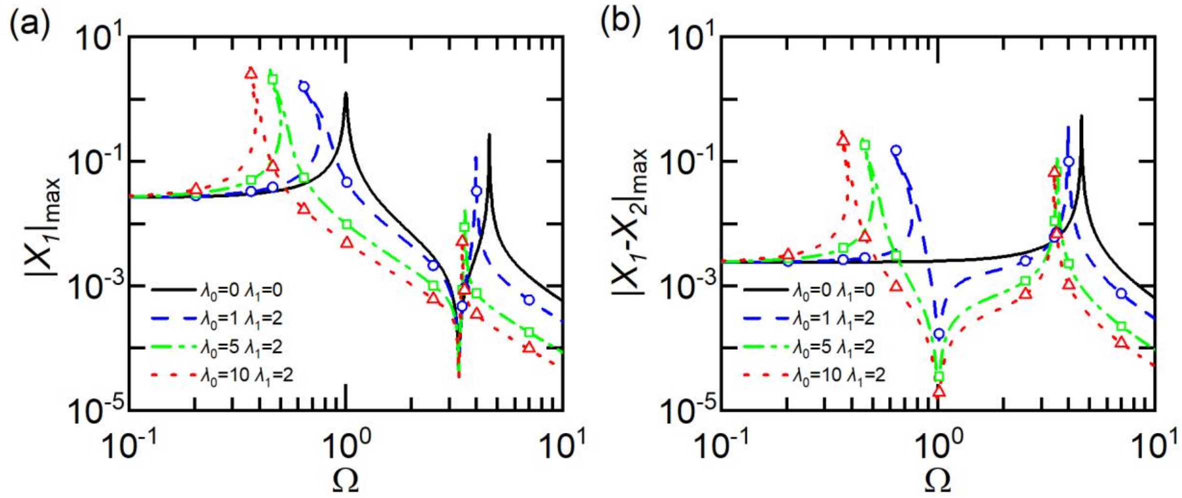

Fig. 15. Effects of the inerter-based nonlinear joint on (a) the response amplitude of mass m_1, and (b) the relative response of masses m_1 and m_2 when the inerter-based joint is added at Q ($\mu = 1, \gamma = 1, \varkappa = 10, \zeta_1 = \zeta_2 = 0.01, F_0 = 0.05$).

In Fig. 16(a) and (b), the influence of the inerter-based nonlinear joint on the time-averaged input power $\bar{P}_{\text{in}}$ and on the transmitted power $\bar{P}_{\text{t}}$ is investigated, respectively. The figure shows that the changes in the inerter-based joint affect $\bar{P}_{\text{in}}$ and $\bar{P}_{\text{t}}$ in a similar way. It shows that from Case one to case two with the addition of the inerter-based joint at position Q, both peaks on each curve of time-averaged power flow shift to the low-frequency range. This behaviour is beneficial for suppression of vibration transmission at high excitation frequencies. The figure shows that the height of the first peak corresponding to the in-phase mode remains almost the same for Cases two, three and four. In contrast, the increase in λ_0 from Case two to four leads to a reduction in the second peak value, which is beneficial for attenuation of vibration transmission. At a prescribed high-frequency range, it shows that Case four leads to the lowest amount of the time-averaged input power and transmitted power. Fig. 16

shows that the first peak of $\bar{P}_{\text{in}}$ and $\bar{P}_{\text{t}}$ bends to the lower frequencies in Case two. With the value of λ_1 increases to 2 as in Case three, there is less bending of the first peak. These characteristics suggest that the inclusion of the inerter-based nonlinear joint is desirable in vibration suppression performance by the reduction of $\bar{P}_{\text{in}}$ and $\bar{P}_{\text{t}}$ over a wide frequency band, both at high frequencies and within the frequency range between two peaks.

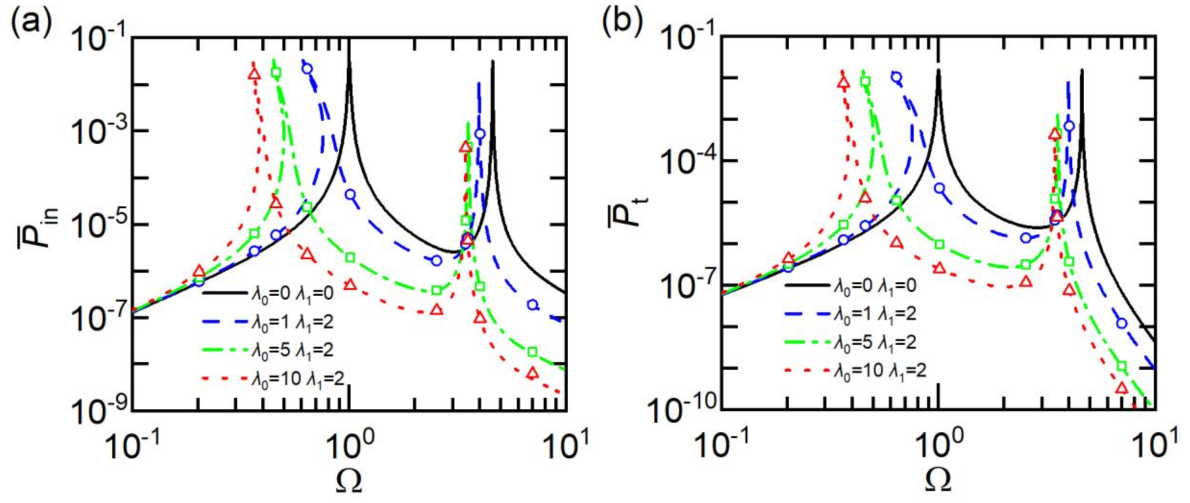

Fig. 16. Effects of the inerter-based nonlinear joint on (a) the time-averaged input power $\bar{P}_{\text{in}}$, and (b) the time-averaged transmitted power $\bar{P}_{\text{t}}$ when the inerter-based joint is added at Q ($\mu = 1, \gamma = 1, \varkappa = 10, \zeta_1 = \zeta_2 = 0.01, F_0 = 0.05$).

Figure 17 presents the effects of adding inerter-based joint at position Q on the force transmissibility TR and the power transmission ratio R_t. Fig. 17(a) shows only one peak in the curve TR for Case one. The use of an inerter-based nonlinear joint with $\lambda_0 = 1, \lambda_1 = 2$ in Case two shifts this peak to the lower frequency and reduces the peak value, compared with Case one. Another peak corresponding to the in-phase mode of the coupled system is introduced at $\Omega \approx 0.64$ in Case two. It is noted that this first peak is bent towards left due to the nonlinear effect introduced by the inerter-based joint. There is an anti-peak found at $\Omega \approx 1$ between the two peaks. The value of force transmissibility at the anti-peak reduces with the inertance λ_0 of the axial inerter, shown by a comparison of Cases two, three and four. The second peak value reduces with the increase of λ_0 and the first one slightly increases with λ_0. The figure shows that the use of the joint device in Case four can lead to much lower value of TR, compared with that of Case one for the original system. These characteristics show the benefits of inerter-based joint in vibration suppression at high frequencies as well as in the vicinity of $\Omega \approx 1$. Fig. 17(b) shows that over the examined range of excitation frequency the power transmission ratio for the four cases tend to merge. In other words, the relative of portion in the total input power that gets transmitted to subsystem two is not sensitive to changes in the inertance λ_0 and λ_1.

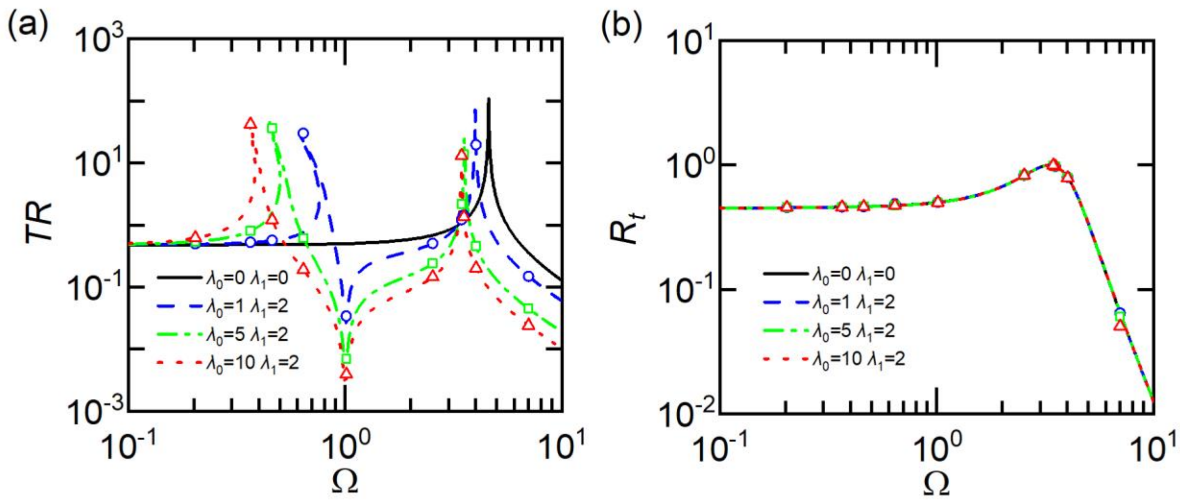

Fig. 17. Effects of the inerter-based nonlinear joint on (a) the force transmissibility TR, and (b) the time-averaged power transmission ratio R_t when the inerter-based joint is added at Q ($\mu = 1, \gamma = 1, \varkappa = 10, \zeta_1 = \zeta_2 = 0.01, F_0 = 0.05$).

6. Conclusions

This study proposed the use of an inerter-based nonlinear joint in a coupled system for the attenuation of vibration transmission between the subsystems. The nonlinear inertance force of the joint device is shown to be dependent on the relative displacement, velocity, and accelerations of its two terminals. The influence of placing the joint device at the interface of the subsystems or within the force-excited subsystem on vibration transmission has been investigated using analytical approximations and numerical integrations. The force transmissibility and time-averaged power flow behaviour were used to access the performance of the inerter-based nonlinear joint. When the inerter-based joint is added to the interface of the subsystems, it was shown that the joint device can significantly reduce the response amplitudes associated with the out-of-phase mode of the system. It was also shown that by the addition of the joint device, the response peaks can be shifted and bent to the low-frequency range for desirable dynamic characteristics. The force transmissibility and power transmission through the interface between the subsystems can be substantially reduced within a prescribed frequency range. It was also demonstrated that inertances of the embed inerters in the joint can lead to the presence of an anti-peak in the curves of force transmissibility, time-averaged transmitted power, and power transmission ratio, and the anti-peak can be placed at interested frequencies to suppress vibration transmission. When the inerter-based nonlinear joint is added to the force-excited subsystem, it was shown that the inclusion of the joint device has large influence on the first peak of the response amplitude corresponding to the in-phase mode, and the extent of the bending increases with the inertance of the lateral inerters. An anti-peak can be found in the curve of force transmissibility, suggesting that the inerter-based nonlinear joint reduces the force transmission at prescribed frequencies. The power transmission ratio from the force-excited subsystem to the other subsystem is not sensitive to the variations in the inertances of the joint. It was also shown that the insertion of the joint device in the system can substantially reduce response amplitude and power transmission, compared to the original system without adding the joint device.

Acknowledgements

This work was supported by National Natural Science Foundation of China [Grant numbers 51605233, 51839005] and by Ningbo Municipal Bureau of Science and Technology under Natural Science Programme [Grant number 2019A610155].

Appendix. Detailed representations of power transmission ratio R_t

When the inerter-based joint is added at position Q, the power transmission ratio R_t from subsystems S1 to S2 is not sensitive to changes in the inertance λ_0 and λ_1 as shown in Figs. 14(b) and 17(b). Here the reasons are demonstrated with mathematical derivations for the case when the inerter-based joint is added at position Q, and the lateral inerters are with $\lambda_1 = 0$. Note that Eq. (6) can be rearranged as:

$$-\Omega^2\tilde{X}_1 + 2\zeta_1 \mathrm{i}\Omega\tilde{X}_1 + \tilde{X}_1 + \kappa\tilde{\Delta} - \Omega^2\lambda_0\tilde{X}_1 = F_0\exp(\mathrm{i}\phi), \tag{39a}$$

$$-\Omega^2\mu\left(\tilde{X}_1 - \tilde{\Delta}\right) + 2\zeta_2\mathrm{i}\Omega\mu\left(\tilde{X}_1 - \tilde{\Delta}\right) + \gamma\left(\tilde{X}_1 - \tilde{\Delta}\right) - \kappa\tilde{\Delta} = 0, \tag{39b}$$

where, $\tilde{X}_1$ and $\tilde{\Delta}$ denotes the complex amplitude of the response of mass m_1 and that of the relative displacement amplitude. According to Eq. (39a) and (39b), the expression of response amplitude can be derived as:

$$\tilde{X}_1 = \frac{F_0\exp(\mathrm{i}\phi)\left(-\Omega^2\mu+2\zeta_2\mathrm{i}\Omega\mu+\gamma+\kappa\right)}{(-\Omega^2+2\zeta_1\mathrm{i}\Omega+1-\Omega^2\lambda_0)(-\Omega^2\mu+2\zeta_2\mathrm{i}\Omega\mu+\gamma+\kappa)+\kappa(-\Omega^2\mu+2\zeta_2\mathrm{i}\Omega\mu+\gamma)}, \tag{40a}$$

$$\tilde{\Delta} = \frac{F_0\exp(\mathrm{i}\phi)\left(-\Omega^2\mu+2\zeta_2\mathrm{i}\Omega\mu+\gamma\right)}{(-\Omega^2+2\zeta_1\mathrm{i}\Omega+1-\Omega^2\lambda_0)(-\Omega^2\mu+2\zeta_2\mathrm{i}\Omega\mu+\gamma+\kappa)+\kappa(-\Omega^2\mu+2\zeta_2\mathrm{i}\Omega\mu+\gamma)}, \tag{40b}$$

$$\tilde{X}_2 = \tilde{X}_1 - \tilde{\Delta} = \frac{F_0\exp(\mathrm{i}\phi)\kappa}{(-\Omega^2+2\zeta_1\mathrm{i}\Omega+1-\Omega^2\lambda_0)(-\Omega^2\mu+2\zeta_2\mathrm{i}\Omega\mu+\gamma+\kappa)+\kappa(-\Omega^2\mu+2\zeta_2\mathrm{i}\Omega\mu+\gamma)}. \tag{40c}$$

The transmitted force to subsystem S2 can be expressed by:

$$\tilde{F}_t = \kappa\tilde{\Delta}. \tag{41}$$

The time-averaged input power and transmitted power over a period of oscillation are:

$$\bar{P}_{\mathrm{in}} = \frac{1}{T}\int_{t_0}^{t_0+T}\mathrm{Re}\{p_{in}\}\,\mathrm{d}t = \frac{1}{2}\mathrm{Re}\{(F_0\exp(\mathrm{i}\phi))^* X_1\mathrm{i}\Omega\}, \tag{42a}$$

$$\bar{P}_{\mathrm{t}} = \frac{1}{T}\int_{t_0}^{t_0+T}\mathrm{Re}\{p_t\}\,\mathrm{d}t = \frac{1}{2}\mathrm{Re}\{\tilde{F}_t^{\,*} X_2\mathrm{i}\Omega\}, \tag{42b}$$

where $*$ denotes the complex conjugate. The power transmission ratio from subsystem one to subsystem two is defined as:

$$R_t = \frac{\bar{P}_{\mathrm{t}}}{\bar{P}_{\mathrm{in}}}. \tag{43}$$

Based on Eqs. (40)-(43), the power transmission ratio R_t can be calculated:

$$R_t = \frac{\bar{P}_{\mathrm{t}}}{\bar{P}_{\mathrm{in}}} = \frac{\kappa^2 2\zeta_2\Omega\mu}{(-\Omega^2\mu+\gamma+\kappa)(-\Omega^2\mu+\gamma+\kappa)2\zeta_1\Omega+2\kappa\zeta_2\Omega\mu\kappa}, \tag{44}$$

where λ_0 is eliminated suggesting that the change in λ_0 will not affect the power transmission ratio from subsystem S1 to subsystem S2.

References

[1] Yang, J., Xiong, Y. P., & Xing, J. T.: Dynamics and power flow behaviour of a nonlinear vibration isolation system with a negative stiffness mechanism. Journal of sound and vibration, 332(1), 167-183 (2013)

[2] Chedjou, J. C., Fotsin, H. B., Woafo, P., & Domngang, S.: Analog simulation of the dynamics of a van der Pol oscillator coupled to a Duffing oscillator. IEEE Transactions on Circuits and Systems I: Fundamental Theory and Applications, 48(6), 748-757 (2001)

[3] Schwingshackl, C. W., Di Maio, D., Sever, I., & Green, J. S.: Modeling and validation of the nonlinear dynamic behavior of bolted flange joints. Journal of Engineering for Gas Turbines and Power, 135(12) (2013)

[4] Jalali, H., Ahmadian, H., & Mottershead, J. E.: Identification of nonlinear bolted lap-joint parameters by force-state mapping. International Journal of Solids and Structures, 44(25-26), 8087-8105 (2007)

[5] Liu, X. C., Cui, F. Y., Jiang, Z. Q., Wang, X. Q., Xu, L., Shang, Z. X., & Cui, X. X.: Tension–bend–shear capacity of bolted-flange connection for square steel tube column. Engineering Structures, 201, 109798 (2019)

[6] Yang, J. S.: Hybrid active and passive control of a very large floating beam structure. Nonlinear Dynamics, 87(3), 1835-1845 (2017)

[7] Stanton, S. C., Culver, D., & Mann, B. P.: Tuning inertial nonlinearity for passive nonlinear vibration control. Nonlinear Dynamics, 99(1), 495-504 (2020)

[8] Smith, M. C.: Synthesis of mechanical networks: the inerter. IEEE Transactions on automatic control, 47(10), 1648-1662 (2002)

[9] Chen, M. Z., Papageorgiou, C., Scheibe, F., Wang, F. C., & Smith, M. C.: The missing mechanical circuit element. IEEE Circuits and Systems Magazine, 9(1), 10-26 (2009)

[10] Glover, A. R., Smith, M. C., Houghton, N. E., & Long, P. J. G.: Force-controlling hydraulic device. International Patent Application No: PCT/GB2010/001491 (2009)

[11] Smith, M. C., & Wang, F. C.: Performance benefits in passive vehicle suspensions employing inerters. Vehicle system dynamics, 42(4), 235-257 (2004)

[12] Li, Y., Jiang, J. Z., & Neild, S.: Inerter-based configurations for main-landing-gear shimmy suppression. Journal of Aircraft, 54(2), 684-693 (2017)

[13] Lazar, I. F., Neild, S. A., & Wagg, D. J.: Using an inerter-based device for structural vibration suppression. Earthquake Engineering & Structural Dynamics, 43(8), 1129-1147 (2014)

[14] Yang, J.: Force transmissibility and vibration power flow behaviour of inerter-based vibration isolators. In Journal of Physics: Conference Series (Vol. 744, No. 1, p. 012234). IOP Publishing (2016)

[15] Yang, J., Jiang, J. Z., Zhu, X., & Chen, H.: Performance of a dual-stage inerter-based vibration isolator. Procedia engineering, 199, 1822-1827 (2017)

[16] Zhu, C., Yang, J., & Rudd, C.: Vibration transmission and power flow of laminated composite plates with inerter-based suppression configurations. International Journal of Mechanical Sciences, 190, 106012 (2020)

[17] Zhang, R., Zhao, Z., Pan, C., Ikago, K., & Xue, S.: Damping enhancement principle of inerter system. Structural Control and Health Monitoring, 27(5), e2523 (2020)

[18] Yang, J., Xiong, Y. P., & Xing, J. T.: Power flow behaviour and dynamic performance of a nonlinear vibration absorber coupled to a nonlinear oscillator. Nonlinear Dynamics, 80(3), 1063-1079 (2015)

[19] Papageorgiou, C., Houghton, N. E., & Smith, M. C.: Experimental testing and analysis of inerter devices. Journal of dynamic systems, measurement, and control, 131(1) (2009)

[20] Papageorgiou, C., & Smith, M. C.: Laboratory experimental testing of inerters. In Proceedings of the 44th IEEE Conference on Decision and Control (pp. 3351-3356). IEEE (2005)

[21] Gonzalez-Buelga, A., Lazar, I. F., Jiang, J. Z., Neild, S. A., & Inman, D. J.: Assessing the effect of nonlinearities on the performance of a tuned inerter damper. Structural Control and Health Monitoring, 24(3), e1879 (2017)

[22] Yang, J., Jiang, J. Z., & Neild, S. A.: Dynamic analysis and performance evaluation of nonlinear inerter-based vibration isolators. Nonlinear Dynamics, 99(3), 1823-1839 (2020)

[23] Yang, J., Shi, B., & Rudd, C.: On vibration transmission between interactive oscillators with nonlinear coupling interface. International Journal of Mechanical Sciences, 137, 238-251 (2018)

[24] Goyder, H. G. D., & White, R. G.: Vibrational power flow from machines into built-up structures, part I: introduction and approximate analyses of beam and plate-like foundations. Journal of sound and vibration, 68(1), 59-75 (1980)

[25] Goyder, H. G. D., & White, R. G.: Vibrational power flow from machines into built-up structures, Part II: Wave propagation and power flow in beam-stiffened plates. Journal of sound and vibration, 68(1), 77-96 (1980)

[26] Goyder, H. G. D., & White, R. G.: Vibrational power flow from machines into built-up structures, Part III: power flow through isolation systems. Journal of Sound and Vibration, 68(1), 97-117 (1980)

[27] Langley, R. S.: Analysis of power flow in beams and frameworks using the direct-dynamic stiffness method. Journal of Sound and Vibration, 136(3), 439-452 (1990)

[28] Clarkson, B. L.: Estimation of the coupling loss factor of structural joints. Proceedings of the Institution of Mechanical Engineers, Part C: Mechanical Engineering Science, 205(1), 17-22 (1991)

[29] Cuschieri, J. M.: Structural power-flow analysis using a mobility approach of an L-shaped plate. The Journal of the Acoustical Society of America, 87(3), 1159-1165 (1990)

[30] Mace, B. R., & Shorter, P. J.: Energy flow models from finite element analysis. Journal of sound and vibration, 233(3), 369-389 (2000)

[31] Wang, Z. H., Xing, J. T., & Price, W. G.: A study of power flow in a coupled plate–cylindrical shell system. Journal of Sound and Vibration, 271(3-5), 863-882 (2004)

[32] Xiong, Y. P., Xing, J. T., & Price, W. G.: Power flow analysis of complex coupled systems by progressive approaches. Journal of Sound and Vibration, 239(2), 275-295 (2001)

[33] Xing, J. T., & Price, W. G.: A power–flow analysis based on continuum dynamics. Proceedings of the Royal Society of London. Series A: Mathematical, Physical and Engineering Sciences, 455(1982), 401-436 (1999)

[34] Ji, L., Mace, B. R., & Pinnington, R. J.: A power mode approach to estimating vibrational power transmitted by multiple sources. Journal of Sound and Vibration, 265(2), 387-399 (2003)

[35] Xiong, Y. P., Xing, J. T., & Price, W. G.: A power flow mode theory based on a system's damping distribution and power flow design approaches. Proceedings of the Royal Society A: Mathematical, Physical and Engineering Sciences, 461(2063), 3381-3411 (2005)

[36] Yang, J., Xiong, Y. P., & Xing, J. T.: Nonlinear power flow analysis of the Duffing oscillator. Mechanical systems and signal processing, 45(2), 563-578 (2014)

[37] Yang, J., Xiong, Y. P., & Xing, J. T.: Vibration power flow and force transmission behaviour of a nonlinear isolator mounted on a nonlinear base. International Journal of Mechanical Sciences, 115, 238-252 (2016)

[38] Krack, M., & Gross, J.: Harmonic balance for nonlinear vibration problems. New York: Springer (2019)

[39] Moussi, E. H., Bellizzi, S., Cochelin, B., & Nistor, I.: Nonlinear normal modes of a two degrees-of-freedom piecewise linear system. Mechanical Systems and Signal Processing, 64, 266-281 (2015)